Four-dimensional numerical modeling of crustal growth at active continental margins

Guizhi Zhu,[1] Taras V. Gerya,[1] Paul J. Tackley,[1] and Eduard Kissling[1]

[1] Crustal growth and topography development in subduction-related arcs are intimately related to magmatic processes and melt production above subducting slabs. Lateral and temporal variations in crustal thickness and composition have been observed in nature, but until now no integrated approach has been developed to comprehensively understand magmatic activity in subduction-related arcs. Here we investigate the 4-D spatial, temporal, and compositional character of continental crustal growth at active margins using a new 4-D (space-time) petrological-thermomechanical numerical model of a subduction-related magmatic arc. Based on a series of numerical experiments, we demonstrate that crustal growth inside the arc is inherently clustered in both space and time. The characteristic wavelength of variations in crustal thickness and topography along the arc is on the order of 30–80 km and is comparable to volcano clustering in natural arcs. The clusters of new crust are formed mainly by basaltic melt episodically extracted from partially molten peridotite due to lateral variation of water release and transport in the mantle wedge. Melts derived from subducted oceanic crust and sediments could contribute up to 15–50 vol% to the arc crust growth and their relative proportion is maximal at the onset of subduction. The total amount of newly formed crust correlates mainly with the amount of convergence since the beginning of subduction and is not strongly influenced by the plate convergence velocity. Indeed, slower subduction and lower melt extraction efficiency helps partially molten sediments and oceanic crust to be transported into the mantle wedge by hydrated, partially molten diapiric structures. For the modeled regime of stable subduction, the maximum crustal additional rate (25–$40 \, km^3/km/Myr$) occurs when the amount of convergence reaches around 700 km. Mantle wedge structures developed in our models correlate well with available geophysical (seismological) observations for the Alaskan subduction zone. In particular, partially molten mantle plumes found in our models could explain low seismic anomalies in the mantle wedge, whereas mobile water and water release patterns could reflect paths and sources for magmatic activity evidenced by seismic b-value and Vp/Vs ratio analysis.

1. Introduction

[2] The formation and growth of continental crust are a subject of long-lasting debate in geophysical [e.g., *Taylor*, 1967; *Reymer and Schubert*, 1984; *Von Huene and Scholl*, 1991; *Rudnick*, 1995; *Albarede*, 1998; *Dimalanta et al.*, 2002; *Hebert et al.*, 2009; *Gerya and Meilick*, 2011; *Vogt et al.*, 2012], petrological [e.g., *Ringwood*, 1990; *Green*, 1980; *Connolly*, 2005], and geochemical [e.g., *Allegre and Othman*, 1980; *Plank and Langmuir*, 1988; *Elliott et al.*, 1997; *Hawkesworth and Kemp*, 2006] literatures. Since the beginning of plate tectonics on the Earth, subduction-related magmatic arcs are considered to be major sites of new continental crust production by plutonic and volcanic processes [e.g., *Aramaki and Ui*, 1978; *Hess*, 1989; *Rudnick*, 1995; *Rudnick and Gao*, 2003; *Ramos-Velazquez et al.*, 2008; *Mortimer et al.*, 2010; *Farris*, 2010; *Maxeine and Rayner*, 2011]. As magmas intrude into the arc crust and erupt to the surface, crust thickens and differentiates as shown by topography [e.g., *Lahitte et al.*, 2012] and seismological profiles [e.g., *Kodaira et al.*, 2006]. Dividing the total volume of arc crust by the time in which it was produced and by the length of the arc, *Reymer and Schubert* [1984] estimated crustal generation rates of 20–$40 \, km^3/km/Myr$ for the western Pacific region during intraoceanic subduction. More recent estimates for the same area by *Stern and Bloomer* [1992] (early stage of Izu-Bonin-Mariana
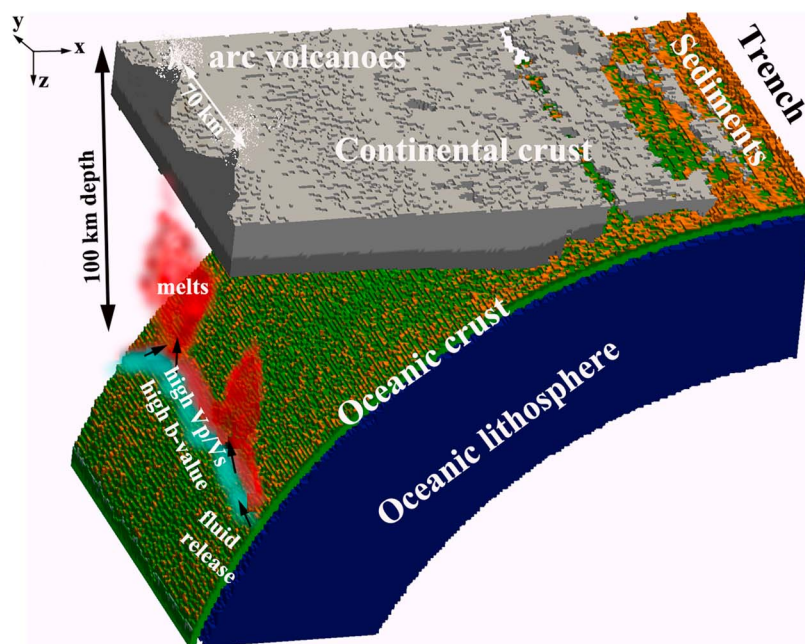
Figure 1. Sketch of clusters of volcanism and fluids/melts in the mantle wedge atop the subducting slab shown in a right-hand coordinate system (x: parallel to plate motion, y: along the trench, z: along the depth). During the subduction of the slab, oceanic crust/sediments/serpentinites dehydrate water and favor partial melt of the mantle wedge atop the slab. Fluid/melts go upward according to local pressure gradient. The presence of fluids/melts can be represented by high Vp/Vs ratio and b-value [*van Stiphout et al.*, 2009]. Colors of composition: Orange: sediments; light grey: upper continental crust; dark grey: lower continental crust; green: basalt; dark green: gabbro; red: partially molten mantle; light blue: hydrated mantle.

development), *Taira et al.* [1998] (Izu-Bonin island arc), *Holbrook et al.* [1999] (Aleutian island arc), and *Dimalanta et al.* [2002] (Tonga, New Hebrides, Marianas, Southern and Northern Izu- Bonin, Aleutian island arcs) are much higher and range from 40–95 km^3/km/Myr to 120–180 km^3/km/Myr.

[3] According to both seismological [e.g.,, *Kodaira et al.*, 2006, 2007] and volcanological [e.g.,, *Tamura et al.*, 2002; *Honda et al.*, 2007] constraints on the distribution of magmatic activity, crustal thickness and composition in arcs are strongly variable in space and time. For example, several authors [e.g., *Tamura et al.*, 2002; *Honda et al.*, 2007; *Zhu et al.*, 2009; *van Stiphout et al.*, 2009] analyzed the spatial distribution of volcanism in Japan and Alaska and concluded that several clusters of volcanism can be distinguished in space and time. As shown in a 3-D representation in Figure 1, the typical spatial periodicity of such volcanic clusters is 50–100 km, whilst their active lifetime is 2–7 Myr. Two trench-parallel lines of maxima in volcanic density can also be distinguished for some periods of arc evolution [e.g., *Tamura et al.*, 2002; *Honda et al.*, 2007, 2010]. *Kodaira et al.* [2007] provided cross-arc lithospheric profiles for the Izu-Bonin intraoceanic arc, which revealed two scales (1000–10 km scale) of variation, one at the scale of the Izu versus Bonin (thick versus thin) arc crust and the other at the intervolcano (~50 km) scale. *Kimura and Yoshida* [2006] presented evidence of petrological variation in time along the NE-Japan arc and proposed different amounts of fluid/melting source parameters atop the subducting slab. *Eiler et al.* [2005] showed that oxygen-isotope compositions of

Central American arc lavas vary systematically along the strike of the arc, from a maximum at the northwest end (Guatemala) to a minimum in the center (Nicaragua), to intermediate values at the southeast end (Costa Rica), which resembles slab dip and crustal thickness. Geochemical compositions of volcanoes at Spur [*Nye and Turner*, 1990; *Nye et al.*, 1995], Augustine [*Roman et al.*, 2006], and Redoubt [*Nye et al.*, 1994] in southern Alaska also show significant geochemical differences along the arc in the southern Alaska subduction zone. Recent 3-D high-resolution tomography further displayed the source and path of these volcanoes along the trench [*van Stiphout et al.*, 2009].

[4] The composition and 3-D structure of arc crust with lateral variations occurring globally [e.g., *Plank and Langmuir*, 1988] are commonly related to dehydration of the slab and hydration and melting of the overlying mantle in subduction zones. Spatial and temporal clustering of volcanic activity is also associated with a strongly variable crustal thickness distribution along arcs [e.g., *Kodaira et al.*, 2006, 2007] and lateral seismic velocity anomalies in the mantle wedges under volcanic arcs [e.g., *Zhao et al.*, 2002; *Zhao*, 2001; *Tamura et al.*, 2002; *Nakajima and Hasegawa*, 2003a, 2003b; *van Stiphout et al.*, 2009]. This further points toward a strong relationship between mantle wedge processes and crustal growth in subduction-related arcs. Consequently, integrated approaches that combine seismic observations, petrochemical observations, and numerical simulations are expected to be necessary for a comprehensive understanding of the 4-D space-time character of magmatic activity and crustal growth.
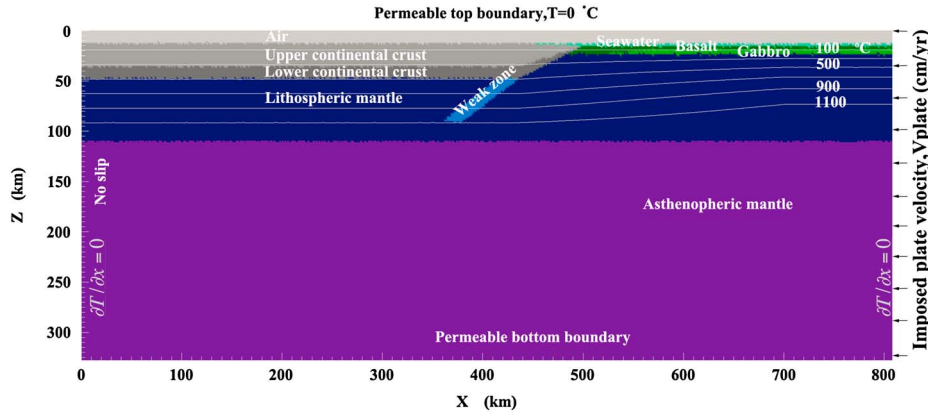
Figure 2. Initial configuration and boundary conditions of numerical model for a lithospheric/upper mantle section (see text (sections 2.1 and 2.2) for details). Isotherms are displayed in white for increments of 200°C, starting from 100°C. Colors of composition: light grey: upper continental crust; dark grey: lower continental crust; light green: sea water; dark green: basalt; green: gabbro; red: partially molten mantle; blue: weak zone.

[5] Until now, little has been done to explore, using numerical thermomechanical models, the 4-D character of crustal growth in volcanic arcs. *Nikolaeva et al.* [2008] investigated crustal growth processes on the basis of a 2-D coupled petrological-thermomechanical numerical model of retreating intraoceanic subduction. They found that the composition of new crust depends strongly on the evolution of subduction. Four major magmatic sources contribute to the formation of the crust: hydrated partially molten peridotite in the mantle wedge, melted subducted sediments, melted subducted basalts, and melted subducted gabbro. Recently, *Vogt et al.* [2012] identified three geodynamic regimes of crustal growth during oceanic-continental subduction related to overriding plate motion, partial melting in the mantle, melt extraction, and melt emplacement in the form of extrusive volcanics and intrusive plutons. *Honda and Yoshida* [2005] explored flip-flop 3-D thermal plumes applicable to Quaternary volcanoes in north-east Japan. *Zhu et al.* [2009, 2011a] examined more complex 3-D petrological-thermomechanical models of intraoceanic subduction focusing on the geometries and patterns of hydrous thermochemical upwellings ("finger-like/sheet-like/wave-like plumes") formed above the slab, and computed spatial and temporal patterns of melt generation rate controlled by the hydrous plume activities. However, previous numerical models did not explore lateral variations in the thickness and composition of newly formed crust, thus leaving a significant gap in reproducing and understanding natural crustal growth processes in subduction-related arcs.

[6] Here, we present the first results from a newly developed 4-D petrological-thermomechanical numerical model of subduction-related magmatic arcs. The model includes imposed convergence of oceanic and continental plates, spontaneous slab bending and accounts for dehydration of subducted crust, aqueous fluid transport, partial melting of mantle wedge, melt extraction, and related crustal and topographic growth within a spontaneously forming magmatic arc. With this new tool, we investigate the 4-D spatial, temporal, and compositional character of continental crustal growth at the intervolcano scale at active margins.

2. Thermal-Chemical Convection Models

2.1. Domain and Initial Setup

[7] The 4-D petrological-thermomechanical model simulates subduction under an active continental margin through time. The spatial domain is a 328 km deep box that is 808 km long orthogonal to the trench and 200 km wide. The origin of the right-handed coordinate system is located at the left-top-back corner of the box. The initial 3-D setup is laterally homogeneous in the y-direction. The lithospheric/upper mantle section is shown in Figure 2. The oceanic crust is represented by a 3 km thick upper layer of hydrothermally altered basalt above a 5 km thick gabbroic section. The oceanic crust does not include sediments, but sediments spontaneously fill the trench after its depth reaches 8 km in order to mimic natural near-trench sedimentation phenomena. The continental crust has a total thickness of 35 km and is composed of 23 km thick felsic upper crust and 12 km thick mafic lower crust. The mantle consists of initially anhydrous peridotite, which can become hydrated by water released from the subducting slab and partially molten as shown Figure 1. For detailed material properties, see Table 1. Subduction initiation is prescribed by a 20 km wide rheologically weak fracture zone at the bottom of continental crust.

[8] The initial temperature field in the oceanic plate is defined by the oceanic geotherm for a 30 Ma lithospheric cooling age [*Turcotte and Schubert*, 2002]. Within the first 98 km depth of the continental plate, the initial temperature field linearly increases from 273 K to 1628 K; then from 98 km depth (in the asthenospheric mantle), an adiabatic gradient of 0.5 K/km is prescribed. Such an initial temperature setup is suitable for modeling subduction zones with young subducting slabs, such as the Alaska subduction zone.

2.2. Boundary Conditions

[9] The thermal boundary conditions are constant temperature (273 K) at the upper boundary, thermally insulating vertical boundaries, and an infinite half space-like condition at the lower boundary [*Gorczyk et al.*, 2007]. This condition allows lateral variation of both temperature and heat flux at the lower boundary in response to subduction.

Table 1. Material Properties Used in Numerical Experiments[a]

Material	Density ($kg\,m^{-3}$)	Thermal Conductivity ($Wm^{-1}\,K^{-1}$)	Rheology E (kJ/mol), A_D ($MPa^{-n}\,s^{-1}$), c (MPa), V (cm^3/mol)	Latent Heat ($kJ\,kg^{-1}$)	Radioactive Heating (μWm^{-3})	$T_{solidus}$ (K)	$T_{liquidus}$ (K)
Sedimentary rocks	2600 (solid) 2400 (molten)	$0.64+807/(T-77)$	Wet Quartzite flow law, $c=1$, $\sin(\phi=0)$, $E=154$, $V=0.0$, $n=2.3$, $A_D=10^{-3.5}$	300	2	$889+179/(P+54)+20200/(P+54)^2$ at $P<1200$ MPa, $831+0.06P$ at $P>1200$ MPa	$1262+0.09P$
Upper continental crust	2700 (solid) 2400 (molten)	$0.64+807/(T-77)$	Wet Quartzite flow law, $c=1$, $\sin(\phi)=0.15$, $E=154$, $V=0.0$, $n=2.3$, $A_D=10^{-3.5}$	300	1	$889+179/(P+54)+20200/(P+54)^2$ at $P<1200$ MPa, $831+0.06P$ at $P>1200$ MPa	$1262+0.09P$
Lower continental crust	2900 (solid) 2400 (molten)	$0.64+807/(T-77)$	Wet Quartzite flow law, $c=1$, $\sin(\phi)=0.15$, $E=238$, $V=0.0$, $n=2.3$, $A_D=10^{-3.5}$	380	0.5	$1327.15+0.0906P$	$1423+0.105P$
Upper oceanic crust (altered basalt)	3000 (solid) 2900 (molten)	$1.18+474/(T-77)$	Wet Quartzite flow law, $c=1$, $\sin(\phi)=0$, $E=154$, $V=0.0$, $n=2.3$, $A_D=10^{-3.5}$	380	0.25	$973-70400/(P+54)+77800000/(P+354)^2$ at $P<1600$ MPa, $935+0.0035P+0.0000062P^2$ at $P>1600$ MPa	$1423+0.105P$
Lower oceanic crust (gabbro)	3000 (solid) 2900 (molten)	$1.18+474/(T-77)$	Plagioclase (An_{75}), $c=1$, $\sin(\phi)=0.2$, $V=0.0$, $E=238$, $n=2.3$, $A_D=10^{-3.5}$	380	0.25	$1327.15+0.0906P$	$1423+0.105P$
Volcanic crust	2800	$1.18+474/(T-77)$	Wet Quartzite flow law, $c=1$, $\sin(\phi=0)$, $E=154$, $V=0.0$, $n=2.3$, $A_D=10^{-3.5}$	380	0.5	$973-70400/(P+54)+77800000/(P+354)^2$ at $P<1600$ MPa, $935+0.0035P+0.0000062P^2$ at $P>1600$ MPa	$1423+0.105P$
Hydrated[b] and serpentinized mantle	3300	$0.73+1293/(T-77)$	Wet Olivine flow law, $c=1$, $\sin(\phi)=0$, $E=470$, $V=0.8$, $n=4$, $A_D=10^{3.3}$	400	0.022	P-T-H_2O dependent melting model of *Katz et al.* [2003]	P-T-H_2O dependent melting model of *Katz et al.* [2003]
Dry mantle	3300 (solid) 2900 (molten)	$0.73+1293/(T-77)$	Dry Olivine flow law, $c=1$, $\sin(\phi)=0.6$, $E=532$, $V=0.8$ $n=3.5$, $A_D=10^{4.4}$	400	0.022	-/-	-/-
References[c]	1,2	3,9	10	1,2	1	4-8	4,8

[a]Other properties (for all rock types): $C_p = 1000$ $Jkg^{-1}K^{-1}$, $\alpha = 3 \times 10^{-5}$ K^{-1}, $\beta = 1 \times 10^{-3}$ MPa^{-1}

[b]Hydrated mantle beyond the antigorite stability field [*Schmidt and Poli*, 1998; $T_k > 751 + 0.18P − 0.0000031P^2$ at $P < 2100$ MPa; $T_k > 1031 − 0.0018P − 0.0000039P^2$ at $P > 2100$ MPa.

[c]1 = *Turcotte and Schubert*, 2002; 2 = *Bittner and Schmeling*, 1995; 3 = *Clauser and Huenges*, 1995; 4 = *Schmidt and Poli*, 1998; 5 = *Hess*, 1989; 6 = *Hirschmann*, 2000; 7 = *Johannes*, 1985; 8 = *Poli and Schmidt*, 2002; 9 = *Hofmeister*, 1999; 10 = *Ranalli*, 1995.
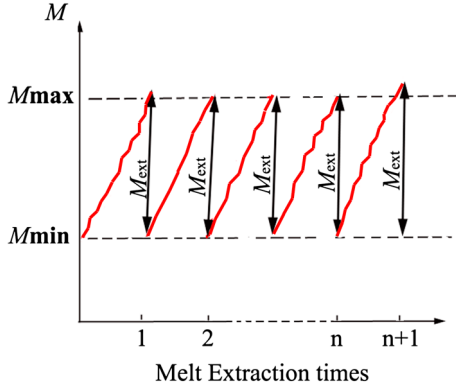
Figure 3. Sketch of melt extraction episodes. Once total amount of melt (M) in the rock is over melt extraction threshold (Mmax), melts are extracted except nonextraction melt fraction (Mmin).

[10] The front and back boundaries are free slip. The left boundary is no slip and the right boundary is also no slip but with the constant prescribed subduction velocity (2.0–6.5 cm/yr). An "external no slip" condition along the lower boundary means that velocities are set to satisfy a no-slip condition at a hypothetical external mechanical boundary located at a depth of 198 km below the bottom of the actual model. This external no-slip condition, which is similar to the usual no-slip condition, allows global conservation of mass in the computational domain and is implemented by the following conditions for velocity components at the lower boundary:

$$\partial v_x/\partial z = -v_x/\Delta z_{externalV}; \quad \partial v_y/\partial z = -v_y/\Delta z_{externalV}; \quad ; \partial v_z/\partial z = -v_z/\Delta z_{externalV} \quad (1)$$

where x is the horizontal coordinate parallel to plate motion, y is the horizontal coordinate along the trench, and z is the vertical coordinate and $\Delta z_{externalV} = 198$ km is the vertical distance from the bottom of the model to the external mechanical boundary where no slip is satisfied. A "sticky air/water" layer [*Schmeling et al.*, 2008; *Crameri et al.*, 2012] with a thickness of 12–15 km is used to impose a free surface condition at the top of the lithosphere. The upper boundary condition is free slip but also accounts for "sticky air" outflow (with constant vertical velocity) in order to balance its continuous input through the right boundary of the model where a constant subduction velocity (i.e., inflow velocity) is prescribed.

2.3. Fluid/Melt Transport Mechanism

[11] To simulate the migration of water released by dehydration, we used independently moving rock and fluid markers [*Gorczyk et al.*, 2007]. The maximum stable water content for each lithology was calculated by free energy minimization [*Connolly*, 2005] as a function of pressure and temperature from thermodynamic data by the Perple_X program [*Connolly*, 2005; *Gerya et al.*, 2006]. The initial water content is zero everywhere except in the basaltic and sedimentary crust where, in addition to mineralogical water, a porous water content is specified as a linear function of depth:

$$X_{H_2O(p)}(wt\%) = X_{H_2O(p_0)}(1 - 0.013\Delta z) \quad (2)$$

where $X_{H_2O(p_0)} = 2$ wt% is the porous water content at the surface, Δz (km) is depth below the surface in km (0–75 km).

The subsequent release of this water also mimics the effects of low-temperature ($<300°C$) reactions that are not included in our thermodynamic database.

[12] A fluid marker with a particular water amount is generated when the local water concentration exceeds the maximum concentration that can be held, and moves upward until it reaches a lithology that assimilates water. Up to 2 wt% of water can be absorbed by hydrated mantle under supersolidus conditions, in agreement with seismic constraints [*Bostock et al.*, 2002; *Carlson and Miller*, 2003]. Solid mantle that could melt with the addition of water can absorb a maximal bulk water content of 0.5 wt%, consistent with typical conditions of fluid-fluxed melting in subduction zones [*Kelley et al.*, 2006].

[13] The velocity of water in the wedge is computed according to pressure gradients [e.g., *Faccenda et al.*, 2009, 2012] as

$$v_{x(water)} = v_x - A\frac{\partial P}{\partial x}$$
$$v_{y(water)} = v_y - A\frac{\partial P}{\partial y}$$
$$v_{z(water)} = v_z - A\left(\frac{\partial P}{\partial z} - \rho_{fluid}g_z\right) \quad (3)$$
$$A = \frac{v_{percolation}}{g_z\left(\rho_{mantle} - \rho_{fluid}\right)}$$

where z is the vertical coordinate with an axis directed downward, x and y are respectively horizontal and lateral (along strike) coordinates; v_x, v_y, and v_z indicate the local velocity of the solid mantle, A is a water percolation constant, $v_{percolation} = 10$ cm/yr, a preassumed standard water percolation velocity, which is in the range of the typical large-scale water transport velocities (1–10 cm/yr) in the mantle wedge [e.g., *Peacock*, 1990; *Gorczyk et al.*, 2007; *Nikolaeva et al.*, 2008], $g_z = 9.81$ m/s^2 is the gravitational acceleration, $\rho_{mantle} = 3300$ kg/m^3 and $\rho_{fluid} = 1000$ kg/m^3 are the densities of the mantle and fluid, respectively. The moving water is consumed by hydration and melting reactions with the mantle located atop the slab.

[14] When the amount of melt reaches the melt extraction threshold, a very fast upward melt migration rate is assumed in all models [e.g., *Hawkesworth et al.*, 1997; *Hall and Kincaid*, 2001; *Nikolaeva et al.*, 2008; *Hebert et al.*, 2009; *Connolly et al.*, 2009]. This instantaneous upward melt movement assumption does not account for lateral melt percolation phenomena driven by horizontal pressure gradients [e.g., *Spiegelman and McKenzie*, 1987]. In a simple way, extracted melt is assumed to be instantaneously removed from the source region to the surface as extrusive volcanics without considering its emplacement underneath the continental crust [*Gerya and Meilick*, 2011; *Vogt et al.*, 2012]. Also, similarly to *Nikolaeva et al.* [2008], we concentrate on fluid-fluxed melting processes atop the slab and do not model shallow decompression melting of the dry mantle under back-arc spreading centers.

2.4. Partial Melting and Melt Extraction

[15] The degree of melting of hydrated peridotite is computed as a function of pressure, temperature, and water content using the parameterization of *Katz et al.* [2003]. The degree of melting of subducted crustal rocks is calculated

Table 2. Description of Selected Numerical Experiments, Among Which Rlinvp Series of Runs Use Water-Saturated P-T Dependent Melting Models for Hydrous Mantle and Others Use P-T-Water Content-Dependent Melting Models

Model	Imposed Plate Velocity (cm/yr)	Melt Extraction Threshold (vol.%)
Rvp65	6.5	4
Rvp5	5.0	4
Rvp3	3.0	4
Rvp2	2.0	4
Brvp5	5.0	6
Brvp3	3.0	6
Brvp2	2.0	6
Rlinvp5	5.0	4
Rlinvp3	3.0	4
Rlinvp2	2.0	4

according to the simpler linear melting model [*Gerya and Yuen*, 2003b; *Zhu et al.*, 2009, 2011a]:

$$M_0 = 0 \text{ at } T < T_{solidus};$$
$$M_0 = (T - T_{solidus})/(T_{liquidus} - T_{solidus}) \text{ at } T_{solidus} < T < T_{liquidus};$$
$$M_0 = 1 \text{ at } T > T_{liquidus}, \tag{4}$$

where M_0 is the volumetric fraction of melt for nondepleted rock with no melt extraction with temperature T, $T_{solidus}$ and $T_{liquidus}$ are, respectively, solidus temperature (wet and dry solidi are used for the hydrated and dry mantle, respectively) and dry liquidus temperature; see Table 1.

[16] The actual melt fraction M is lower than M0 because melt is extracted. For model simplicity, the melt extraction threshold in our model is the same for all types of melt. Although it can be lower for low-viscosity basaltic melts, it can be notably higher for the more viscous granitic and dacitic melts present in our models. *Faul* [2001] has shown that a deep, volatile-rich melt with low viscosity and density is mobile at 0.1% porosity, but basaltic melt only becomes mobile at a porosity above 1%. *Nikolaeva et al.* [2008] have varied melt extraction threshold from 0.2 to 30% melt fraction to find its influence on crust production. Here we use an intermediate value for the melt extraction threshold M_{max} of 4% or 6% and a nonextractable melt fraction (that remains in the source region) M_{min} of 2% or 3%, similar to previous 2-D models [*Nikolaeva et al.*, 2008; *Gerya and Meilick*, 2011; *Vogt et al.*, 2012]. The amount of melt extraction is tracked by markers during the evolution of each experiment. In order to avoid over-extraction of melts from the moving rock markers and keep nonextractable melt in the mantle, the total amount of available melt, M, for every marker takes into account previously extracted melt and is calculated as:

$$M = M_0 - \sum_n M_{ext} \tag{5}$$

where $\sum_n M_{ext}$ is the total melt fraction extracted during the previous n extraction episodes. In our model, the rock is considered nonmolten (refractory) when the extracted melt fraction is larger than the standard one (i.e., when $\sum_n M_{ext} > M_0$). In the case that the total amount of melt M exceeds the threshold M_{max}, the melt fraction $M_{ext} = M - M_{min}$ is extracted and $\sum_n M_{ext}$ is updated. After each melt extraction episode, only nonextractable melt remains in the source region ($M = M_{min}$). Starting from this moment, the total amount of melt M in the

source region varies dynamically according to equations (4) and (5) until it again reaches the M_{max} threshold and another melt extraction episode takes place. This is schematically presented in Figure 3. The extracted melt fraction M_{ext} is assumed to propagate upward to the surface much faster than the mantle rocks deform [*Elliott et al.*, 1997; *Hawkesworth et al.*, 1997]. Hence, the instantaneous transmission of extracted melt to the surface is reasonable. At the surface, extracted melt markers create a volcanic arc and thereby retain their volume and composition. The effective density, ρ_{eff}, of partially molten rock is calculated from

$$\rho_{eff} = \rho_{solid}\left(1 - M + M\frac{\rho_{0molten}}{\rho_{0soild}}\right) \tag{6}$$

where ρ_{0soild} and $\rho_{0molten}$ are the standard densities of solid and molten rock respectively (Table 1) and ρ_{solid} is the density of solid rocks at given P (MPa) and T(K) computed from

$$\rho_{solid} = \rho_{0soild} \times [1 - (\alpha_{molten}M + \alpha_{solid}(1 - M))(T - 298)] \\ \times [1 - (\beta_{molten}M + \beta_{solid}(1 - M))(P - 0.1)] \tag{7}$$

where α, β represent thermal expansion and compressibility of rocks shown in Table 1. Due to the applied melt extraction, the actual density difference between solid and partially molten rocks is rather small in our models.

2.5. Rheological Model

[17] The viscosity in our models depends on strain rate (defined in terms of deformation invariants), pressure, and temperature according to standard experimentally determined flow laws [*Ranalli*, 1995] as:

$$\eta_{creep} = (\dot{\varepsilon}_{II})^{(1-n)/2n}(A_D)^{-1/n}\exp\left(\frac{E_a + PV_a}{nRT}\right) \tag{8}$$

where $\dot{\varepsilon}_{II} = 1/2\,\dot{\varepsilon}_{ij}\dot{\varepsilon}_{ij}$ is the second invariant of the strain rate tensor and A_D, E_a, V_a, and n are experimentally determined flow law parameters (Table 1).

[18] The ductile rheology is combined with a brittle/plastic rheology to yield an effective visco-plastic rheology. For this purpose, the Drucker-Prager yield criterion [*Ranalli*, 1995] is implemented by a limiting creep viscosity, η_{creep}, as follows:

$$\eta_{creep} \le \frac{c + P\sin(\phi)}{(4\dot{\varepsilon}_{II})^{1/2}} \tag{9}$$

where P is the complete (nonlithostatic) pressure (i.e., the mean stress), c is the cohesion (residual strength at $P = 0$), and ϕ is the effective internal friction angle (Table 1). Assuming high pore fluid pressure in hydrated rocks [*Gerya et al.*, 2008], the upper oceanic crust (basalts, sediments) are characterized by $c = 1$ MPa, $\sin\phi = 0$.

2.6. Numerical Solution Method

[19] For performing numerical experiments, we used the recently developed 3-D petrological-thermomechanical modeling code I3ELVIS [*Gerya and Yuen*, 2007], which uses a marker-in-cell method with velocity and pressure discretized using conservative finite differences (finite volume) [*Gerya and Yuen*, 2003a] and a multigrid solver. The governing equations are given in section A1 and parameters description is listed in Table A1. A new addition is the melting model of *Katz et al.* [2003]] for hydrous mantle. The modeling
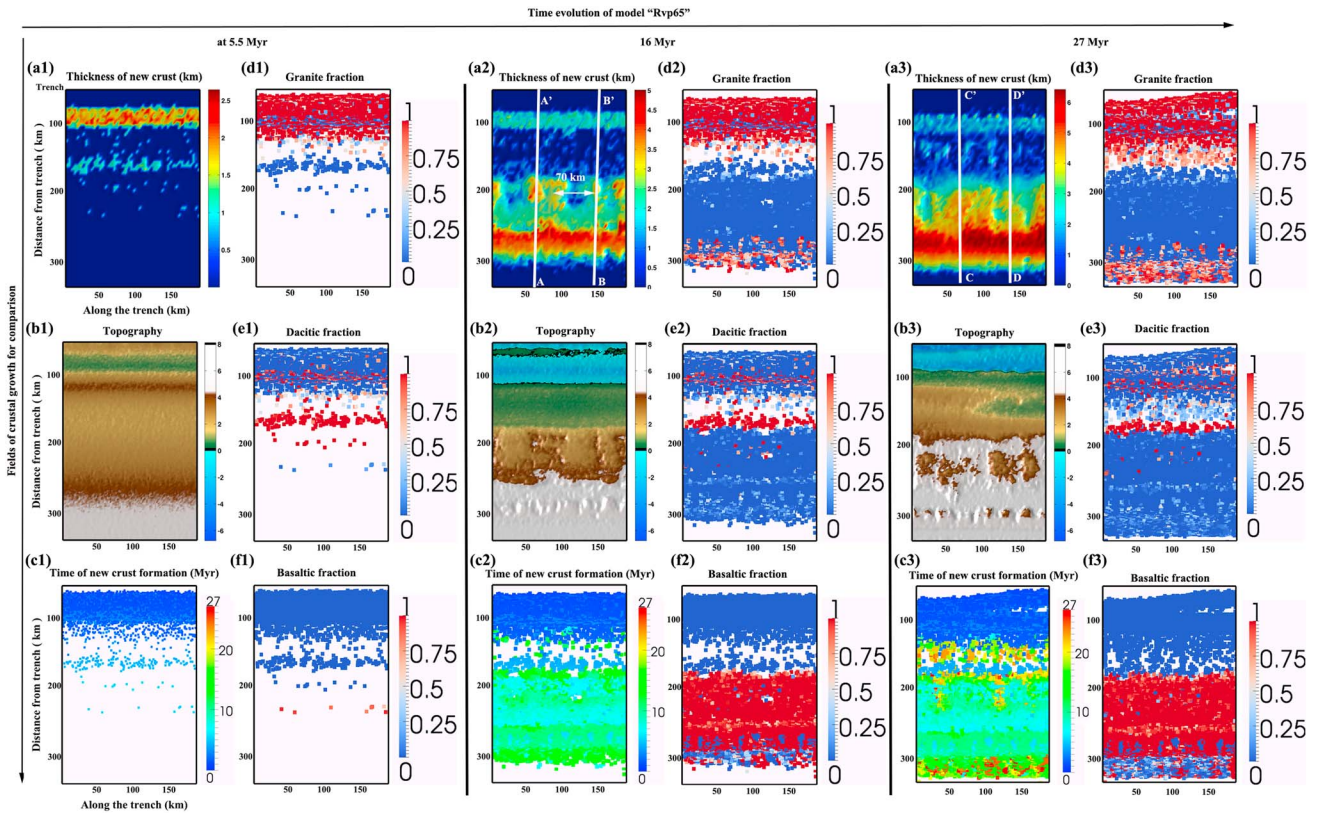
Figure 4. Development of crustal growth in Model "Rvp65" (subduction velocity of 6.5 cm/yr) at 5.5 Myr (1: left panel), 16 Myr (2: middle panel), and 27 Myr (3: right panel). Shown in the panels are, respectively, thickness of new crust (a1, a2, a3), topography (b1, b2, b3), time of new crust formation (c1, c2, c3), granite fraction (d1, d2, d3), dacite fraction (e1, e2, e3), and basalt fraction (f1, f2, f3) of the newly formed crust. Lines AA′, BB′, CC′, and DD′ shown in Figures 4a2 and 4a3 indicate the locations of vertical mantle wedge profiles AA′, BB′, CC′, and DD′ in Figure 6. There are three types of newly formed crust, whose distribution varies along the trench with a wavelength of 50–70 km. Topography grows rapidly as a result of crustal thickening along the time. More is detailed in text sections 3.1 and 3.2.1. Note that in order to highlight the lateral variations of crustal thickening at each time step, we use a scale of 0 – maximal values at each time step rather than a uniform scale.

domain is resolved by $405 \times 165 \times 101$ grid points, which implies grid cell size of $2 \times 2 \times 2$ km comparable to previous 2D subduction models [e.g., *Nikolaeva et al.*, 2008; *Gerya and Meilick*, 2011; *Vogt et al.*, 2012; *Faccenda et al.*, 2012]. The effective resolution of the marker field is 1 km (eight markers per grid cell). Lithologically, 3 km thick basalt crust is thus resolved with 1.5 cells and six markers, which is enough to localize deformation in basaltic crust along the plate interface [*Gerya and Meilick*, 2011; *Faccenda et al.*, 2012]. Two-dimensional resolution tests for this type of subduction model are presented elsewhere [*Faccenda et al.*, 2012; *Naliboff et al.*, 2013].

3. Results

[20] This paper is the first to model and investigate spatial and temporal variations of crustal growth in a 3-D active subduction margin caused by flux melting dependent on pressure, temperature, composition, and water content. Here we focus on the influence of subduction velocity and melt extraction efficiency on 4-D crustal growth. Thus, a series of runs with different subduction velocities in the range 2.0–6.5 cm/yr and

a melt extraction threshold of 4% and 6% are performed, as listed in Table 1. Model "Rvp65," which has an imposed plate velocity of 6.5 cm/yr and melt extraction threshold of 4%, is regarded as the reference model (Table 2).

[21] In the following sections, we analyze the development of crustal thickness, topography, and new crust fraction for models "Rvp65" (Figure 4) and "Rvp2" (Figure 5). We investigate the correlations between composition in the mantle wedge, degree of melt extraction, melt extraction rate, concentration of mobile water, and water release rate for these two models (Figures 6 and 7). These trench-perpendicular vertical profiles intersecting locations with relatively higher crust growth clearly show the lateral variations of 3-D dynamics of mantle wedge. Moreover, we analyze the amount of magmatic rock and crustal addition rate during subduction for cases with different subduction velocities and melt extraction efficiencies (Figure 8). It is noteworthy that our previously used "linear melting model" [*Zhu et al.*, 2009, 2011a] and the "Katz melting model" produce quantitatively different amounts of new crust (cf. Figures 8b1 and 8e1 and Figure 9), but the results are still qualitatively consistent, as discussed in the Discussion section.
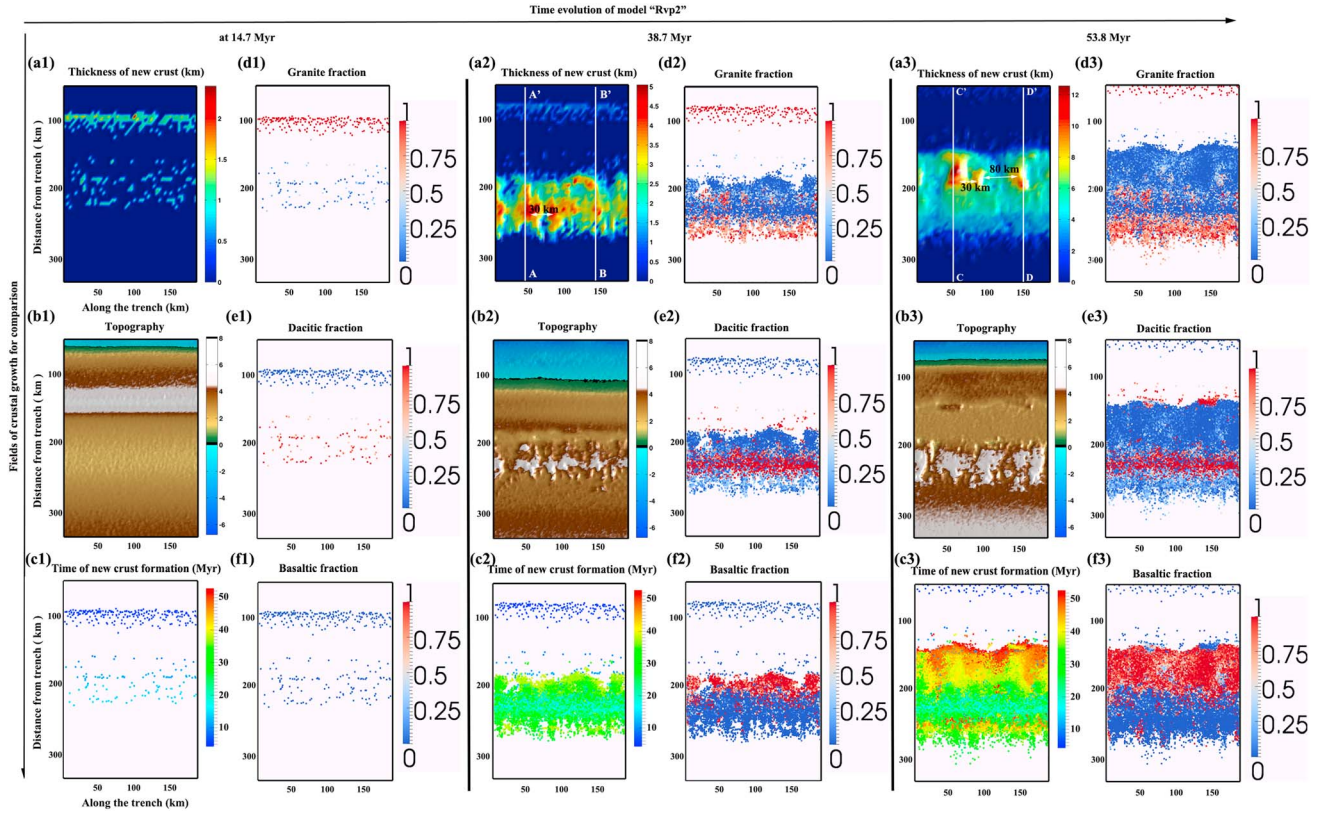
Figure 5. Development of crustal growth in Model "Rvp2" (subduction velocity of 2.0 cm/yr) at 14.7 Myr (1- left panel), 38.7 Myr (2 - middle panel), and at 53.8 Myr (3 - right panel). Shown in the panels are thickness of new crust (a1, a2, a3), topography (b1, b2, b3), time of new crust formation (c1, c2, c3), granite fraction (d1, d2, d3), dacite fraction (e1, e2, e3), and basalt fraction (f1, f2, f3) of the newly formed crust. Lines AA′, BB ′, CC′, and DD′ shown in Figures 5a2 and 5a3 indicate the locations of vertical mantle wedge profiles in Figure 7. The distribution of these three types of newly formed crust varies strongly along the trench, with a wavelength of 30–80 km at 38.7 Myr when it gets similar convergence amount to model "Rvp65" at 16 Myr. More is detailed in text sections 3.1 and 3.2.1. Note that in order to highlight the lateral variations of crustal thickening at each time step, we use a scale of 0 – maximal values at each time step rather than a uniform scale.

3.1. Common 3-D Characteristics of Newly Formed Crust and Topography Versus Time

[22] During the subduction of oceanic lithosphere beneath the overriding continental plate, the distribution of three types of newly formed crust (i.e., granitic, dacitic, and basaltic) varies in space and time (see Figures 4d, 4e, and 4f and Figures 5d, 5e, and 5f). According to our model, granitic crust is produced by melt extraction from partially molten sediments and upper continental crust. Dacitic crust is produced by partially melting gabbros, basalts, and continental lower crust. Basaltic crust is produced by partially melting peridotite. All of these contribute to the accumulation of new crust (Figure 4a and Figure 5a) and topography development (Figures 4b and 5b).

[23] The volume of newly formed crust positively correlates with the duration of subduction. One possible complexity is that continental crust close to the trench might be recycled into the mantle by subduction [e.g., *Staudigel et al.*, 1981] or by delamination of the lower crust [e.g., *Rudnick and Gao*, 2003]. In this study, we do find that some new crust close to the trench (produced less than 2 Myr since the beginning of the calculation)

can be easily subducted into the mantle wedge. Thus, early-formed crust (formed in the first 2 Myr of the calculation) is not included in the calculation of new crustal thickness. Comparing Figures 4a1 and 4a2 and Figure 4a3 for model "Rvp65," the thickness of the new crust increases with time. Consequently, topography grows rapidly as a result of this crustal thickening (see Figures 4b1, 4b2, and 4b3). Note that in order to highlight the lateral variations of crustal thickening at each time step, we use a scale of 0 – maximal values at each time step rather than a uniform scale.

[24] At the onset of the subduction (at 5.5 Myr shown in Figure 4(a–f)1), sediments and continental crust at the active margin are first subducted along the slab then become partially molten at shallow depth with the help of expelled water. The newly formed crust is mostly granitic and forms a linear pattern close to the trench (Figure 4d1). Some dacitic crust gradually forms at a slightly greater distance from the trench because of the partial melting of subducted gabbros and basalts (Figure 4e1) and basaltic crust appears sporadically even farther from the trench (Figure 4f1, and Figure 5f1). At 16 Myr and 27 Myr, production of granitic and dacitic crust still continues because of the partial melting of newly subducted sediments and
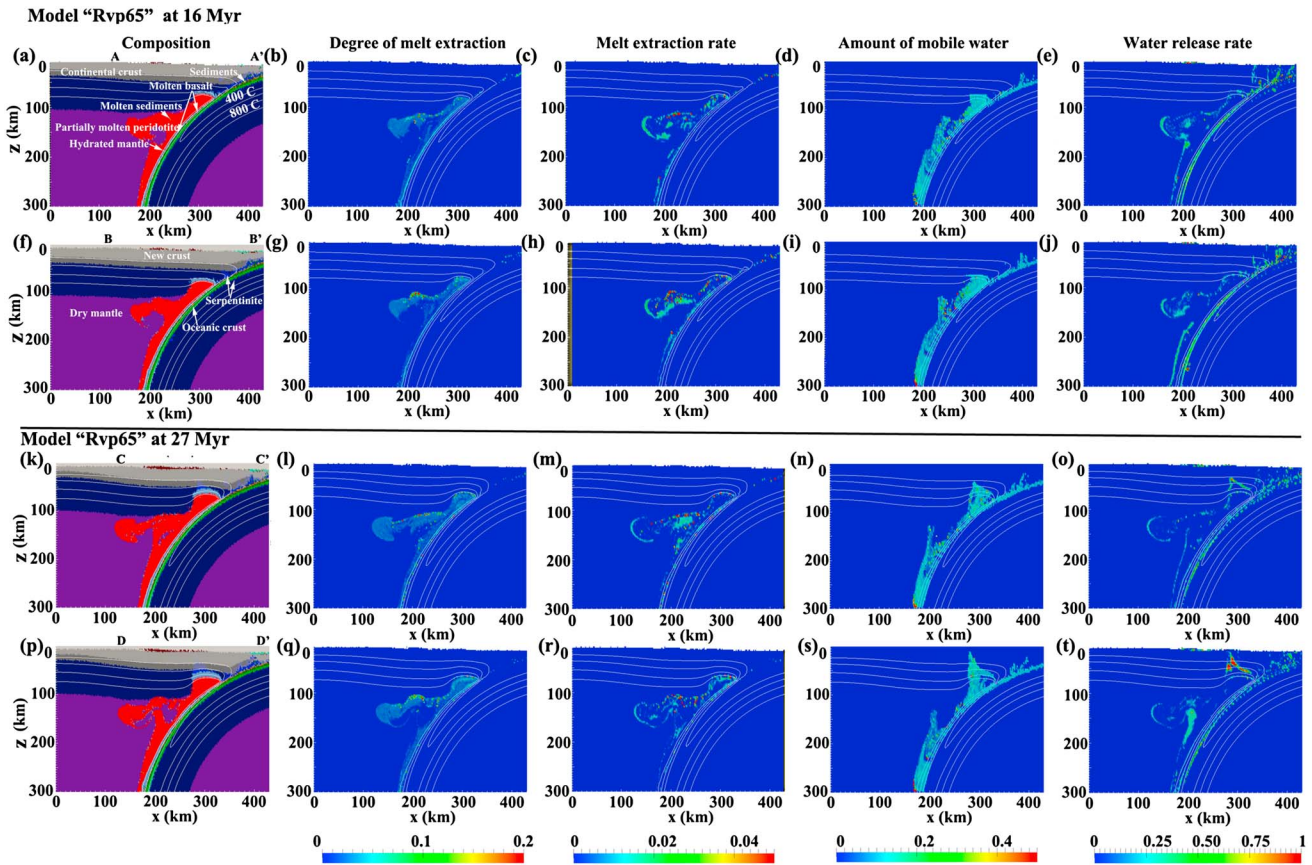
Figure 6. Vertical sections showing mantle wedge dynamics for Model "Rvp65" subduction velocity of 6.5 cm/yr) at (a–j) 16 Myr and (k–t) 27 Myr. The locations of the sections are shown in Figure 4. Vertical sections show composition (first column), degree of melt extraction (second column), melt extraction rate (third column, in 1/Ma), concentration of mobile water (fourth column, in weight%), and water release rate (fifth column, in weight%/Ma). Note that the water release rate is defined by the positive water concentration change in the mantle wedge between two time steps. Colors of composition: Orange: sediments; light grey: upper continental crust; dark grey: lower continental crust; green: basalt; dark green: gabbro; red: partially molten mantle; blue: serpentinite; light blue: hydrated mantle; brown: new crust; violet: dry mantle. Cross sections at peaks of new crust show lateral variation of hydration/melting region in the mantle wedge (first, second, third columns) and the corresponding source and path of magmatic activities in the mantle wedge (fourth and fifth columns). See sections 3.2.2 and 3.3.3 for more details.

oceanic crust (compare Figures 4d1–e1, 4d2–e2, and 4d3–e3). In contrast, there is a very large increase in the thickness of basaltic crust (compare Figures 4f1, 4f2, and 4f3) due to the large amount of partially molten peridotite (Figure 6). Similar features can be found for model "Rvp2" shown in Figure 5f3.

[25] Basaltic crust is extracted quite unevenly along the trench and causes prominent 3-D patterns of clusters. Figures 4a2 and 4a3 show clusters of new crust with a wavelength of around 70 km, ~100–200 km from the trench. Topography also shows a similar scale (Figures 4b2 and 4b3). We note that our models overestimate the magnitude of topography due to neglecting surface erosion processes.

3.2. 4-D Crustal Growth

3.2.1. Development of Clusters of the Newly Formed Crust Along the Trench

[26] Crustal growth in response to arc volcanism is closely related to subduction dynamics. Several studies have explored the relationships between volcanism and measurable subduction parameters including convergent rate, slab dip angle, age of subducting lithosphere [e.g., *Syracuse and Abers*, 2006; *England and Katz*, 2010], and the crustal thickness of the overriding plate [e.g., *Plank and Langmuir*, 1988]. In agreement with our previous 2-D studies on the dynamics of crustal growth [*Nikolaeva et al.*, 2008], the amount of newly formed crust depends on the subduction plate velocity and the efficiency of melt extraction. Our 3-D models presented here can further indicate how 3-D features (and 2-D surface distributions) respond to these two parameters.

[27] With a similar convergence amount, defined by subduction velocity times duration of subduction (the units used here are km, km/Myr, and Myr, respectively), the wavelength or lengthscale of variations in the thickness of new crust and corresponding topography along the trench are on the order of 30–80 km (cf. Figures 4 and 5). Figure 5b3 also shows that crustal growth clusters are not always correlated with the topography growth (Figures 5(c–f)3): at distances of less than 200 km away from trench, topography relaxation above the deforming accretionary wedge seems to completely obliterate volcanic crustal growth signatures.
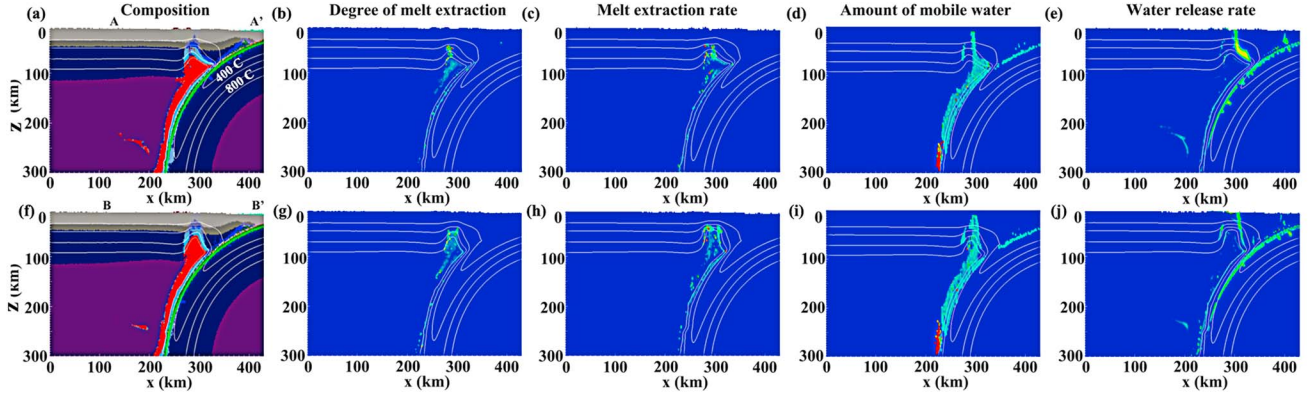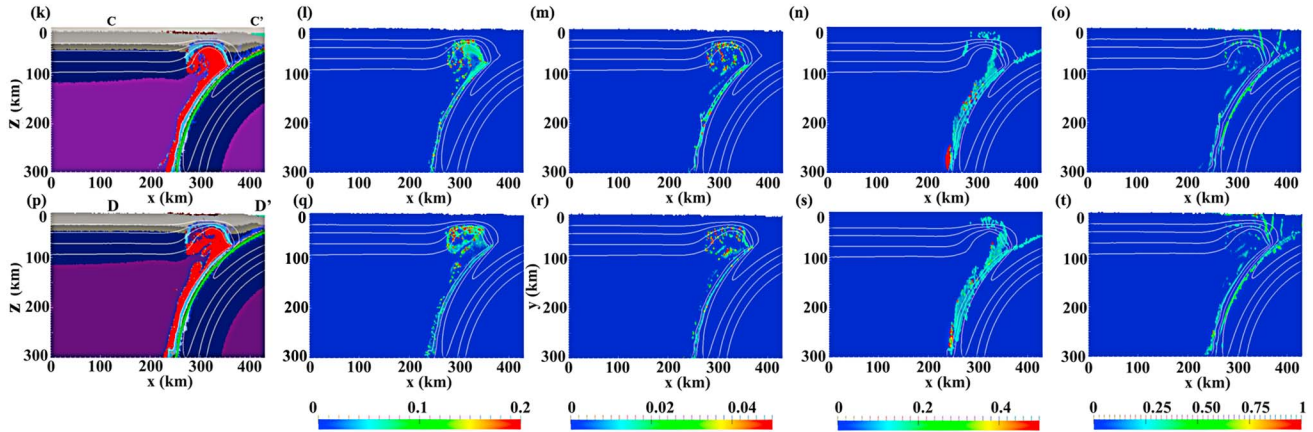
Figure 7. Vertical sections showing mantle wedge dynamics for Model "Rvp2" subduction velocity 2.0 cm/yr) at 38.7 Myr and 53.8 Myr. The locations of profiles AA′, BB′, CC′, and DD′ are shown in Figure 5.Vertical sections show composition (first column), degree of melt extraction (second column), melt extraction rate (third column, in 1/Ma), concentration of mobile water (fourth column, in weight%), and water release rate (fifth column, in weight%/Ma). Note that the water release rate is defined by the positive water concentration change in the mantle wedge between two time steps. Colors of composition: Orange: sediments; light grey: upper continental crust; dark grey: lower continental crust; green: basalt; dark green: gabbro; red: partially molten mantle; blue: serpentinite; light blue: hydrated mantle; brown: new crust; violet: dry mantle. Cross sections at peaks of new crust show lateral variation of hydration/melting region in the mantle wedge (first, second, and third columns) and the corresponding source and path of magmatic activities in the mantle wedge (fourth and fifth columns). Compared to Figure 6, it shows that subduction velocity influences the size of hydration/melting region in the mantle wedge, the depth of melt extraction, and water release. See sections 3.2.2 and 3.3.3 for more details.

3.2.2. Lateral Variation of Hydration/Melting Region in the Mantle Wedge

[28] It is accepted that hydration of the mantle wedge caused by the dehydration of the slab favors the melting of peridotite mantle [e.g., *Iwamori*, 1998; *Katz et al.*, 2003; *Grove et al.*, 2006]. As the slab subducts, water is expelled from the oceanic crust by compaction and dehydration reactions at shallow depth. Thus, serpentinized or hydrated overlying mantle wedge is formed due to hydration, and this favors further melting. Our 3-D results indicate lateral variations of composition, degree of melt extraction, melt extraction rate (which is related to the amount of mobile water), and water release rate in the mantle wedge (Figures 6 and 7).

[29] Vertical profiles of composition located at magmatic clusters along lines AA′ and BB′ in Figure 4a2 and lines CC′ and DD′ in Figure 4a3 for a higher subduction velocity

of 6.5 cm/yr (model "Rvp65") show that the extent of the partially molten mantle region controls the horizontal distribution of new crust at the surface with time (first column in Figure 6). Profiles AA′ and BB′ at 16 Myr show some lateral variation in the form of the partially molten plumes mixing with molten sediments and oceanic crust. They also show differences in upwardly moving and underplating plumes (compare profiles CC′ and DD′ of Figure 6 at 27 Myr) along the trench. The degree of melt extraction (shown in the second column in Figure 6) also shows lateral variation along the trench at a specific time (see AA′ and BB′ profiles at 16 Myr; CC′ and DD′ profiles at 27 Myr). The melt extraction rate outlines the envelope of the partially molten plumes (see the third column in Figure 6). BB′ has more intense extraction compared to AA′, and CC′ has higher melt extraction than DD′ (Figure 6).
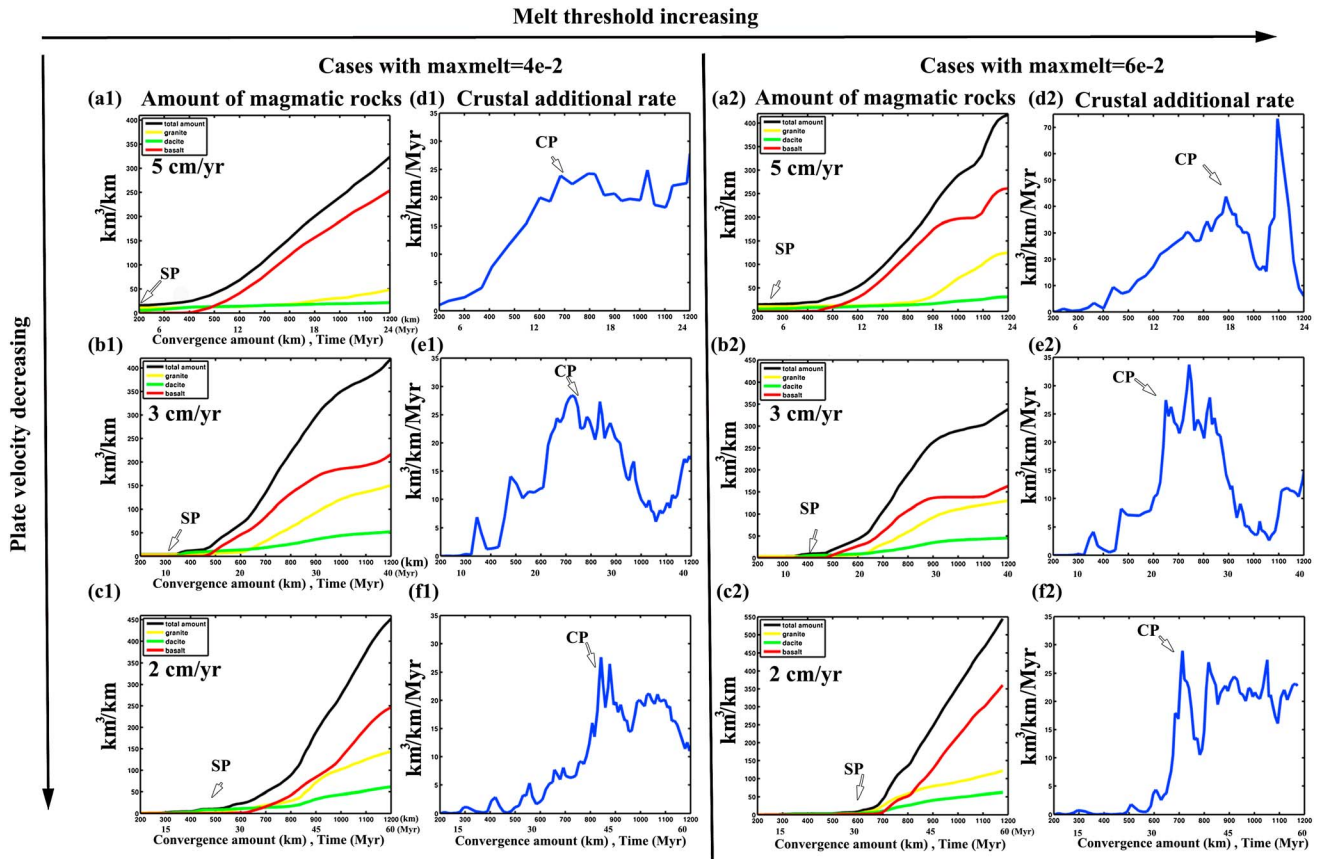
Figure 8. Influences of different melt threshold (maxmelt = 4% in the left panel and maxmelt = 6% in the right panel) and different subduction rate (5.0, 3.0, and 2.0 cm/yr, respectively) on the generated amount of magmatic rocks (a1, b1, c1; a2, b2, c2) and crustal addition rate (d1, e1, f1; d2, e2, f2) for the same convergence amounts (calculate as time*subduction rate). It shows the influence of plate velocity and melt threshold on the amount of magmatic rocks and crustal additional rate. See text section 3.3.

[30] Changing the subduction velocity results in notable differences in the depths of plumes and in plume dynamics, as indicated by fields of composition, melt extraction, melt extraction rate, amount of mobile water, and water release plotted for the two cases "Rvp65" and "Rvp2" in Figures 4 and 5. After a similar amount of convergence, a subducting slab with a subduction velocity of 6.5 cm/yr (Figure 6) can more efficiently carry oceanic crust and serpentinites down the subduction zone [e.g., *Tatsumi*, 1989; *Arcay et al.*, 2005; *Nikolaeva et al.*, 2008; *van Keken et al.*, 2011] than a slab with a smaller velocity of 2.0 cm/yr (Figure 7). Thus, the depth of dehydration is deeper and the depth range of the mantle column between the dehydrating slab and the overlying crust is greater [e.g., *Plank and Langmuir*, 1988; *Arcay et al.*, 2005] which favors a wider area of hydration and melting. In contrast, model "Rvp2" has narrow partially molten plumes starting at shallower depth (first column in Figure 7). This is because, due to the much slower subduction velocity in model "Rvp2," there is more time for plumes (containing oceanic crust and sediments) to develop in the mantle wedge. Moreover, profiles AA′ and BB′ (Figure 7) also show lateral variations in composition, degree of melt extraction, and melt extraction rate at 39 Myr for model "Rvp2." The plume head develops more complexity by 54 Myr (profiles CC′ and DD′). Slower subduction velocity results in a tendency for plumes to penetrate through the

hydrated continental lithosphere (model "Rvp2"), rather than underplating the lithosphere (compare Figures 6a and 7a). The spatial distribution of melt extraction rate in "Rvp2" (Figure 7, third column) shows that melt extraction occurs almost evenly inside the plume of partially molten rocks contributing to the new crust.

3.2.3. Lateral Variations of the Source and Path of Magmatic Activity

[31] The explanation for the location of volcanic arcs remains in debate. Recently, *Grove et al.* [2009] proposed that kinematic variables and water transport control the formation and location of arc volcanoes. *England and Katz* [2010] argued that the arc is located above the place where the boundary defined by the anhydrous solidus makes its closest approach to the trench. In this study, we analyze 3-D variations in the concentration of mobile water and water release rate in the subduction zone, which reflect the path and source of the fluids/melts in the mantle wedge [e.g., *Zhu et al.*, 2011b]. Profiles of the mobile water concentration and water release rate for the reference model "Rvp65" and the slow-subduction-velocity model "Rvp2" are shown in the fourth and fifth columns of Figures 6 and 7, respectively. These profiles of water distribution are rather similar to our previous 2-D results [e.g., *Nikolaeva et al.*, 2008] but differ in some details from some of the other 2-D subduction models [e.g., *Cagnioncle et al.*, 2007; *Hebert et al.*, 2009].
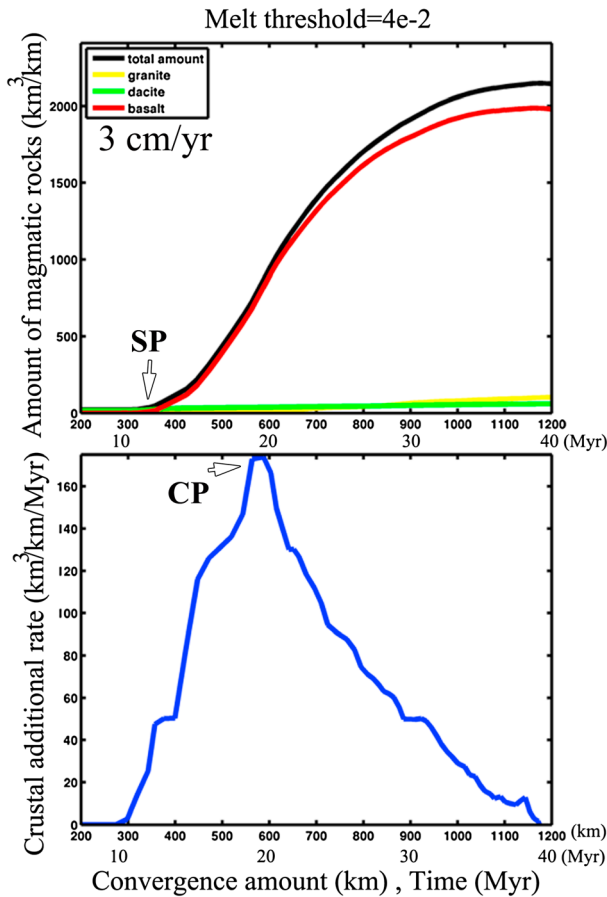
Figure 9. Amount of magmatic rock and crust addition rate for the case with a linear melting model for hydrous mantle. Comparison to Figures 8b1 and 8e1 shows the strong influence of the melting model on the generated amount of magmatic crust.

These discrepancies are mainly due to the differences in the initial water distribution inside the slab and the peculiarities of water transport algorithms adopted in different models.

[32] Mobile water released from the slab causes the formation of serpentinized mantle and hydrated mantle (dependent on the (p, T) conditions), and in situ partial melting of the mantle. Partially molten rock has a low mobile water content because a large amount of water can be contained in the melt. We observe that the maximum in the mobile water concentration (fourth column in Figures 6 and 7) is below the maximum of melt extraction (second column in Figures 6 and 7) and above the area with a high water release rate (fifth column in Figures 6 and 7). This indicates the relationship between melt extraction, path, and source of the fluids/melts in mantle wedge. The water is released by subducted oceanic crust and serpentinites. As the slab subducts, partially molten plumes propagate toward the mantle corner while subducted crust still goes down together with subducting slab. At 27 Myr, profile CC′ (Figure 6) has two regions with a high mobile water concentration released by subducted oceanic crust, which is also indicated by the profiles of water release rate. One region is at the mantle wedge corner, and the other one is deeper than that in profiles AA′ and BB′. It is noteworthy that a major hydrated mantle front containing relatively high mobile water

concentration is formed at the bottom edge of the serpentinite layer with an isotherm of 550°C [*Faccenda et al.*, 2012]. Profile DD′ has similar features to profile CC′, but the depth range of mobile water differs, which may be caused by lateral variations in plume development.

[33] Model "Rvp2" with the slower subduction velocity also displays lateral variations in amount of mobile water (fourth column in Figure 7) and water release rate (fifth column in Figure 7). Compared to Figure 6, water release for model "Rvp2" in Table 1 occurs intensely in a narrow region closer to the trench at shallower depth. The slab in this model subducts more slowly and becomes steeper and hotter at the same amount of convergence compared to the reference model "Rvp65."

3.3. Influence of Subduction Velocity and Melt Extraction Efficiency on the Volume of New Crust Over Time

[34] In this section, we investigate the influence of subduction velocity and melt extraction efficiency on the volume of new crust and the crustal addition rate. We focus on the relationship between the volume of magmatic rock/crustal addition rate and the amount of convergence, as a function of imposed plate velocity (see Figure 8—top row: 5.0 cm/yr; middle row: 3.0 cm/yr; bottom row: 2.0 cm/yr), with different melt extraction thresholds of 4% (left panel) and 6% (right panel).

[35] From these graphs, we distinguish a starting point (**SP**) after which the volume of newly formed crust starts to increase rapidly. After this **SP**, subduction velocity does not have a strong influence on the total volume of newly formed crust, but it has a strong effect on the relative amounts of different components of the crust (granite, dacite, and basalt). Figure 8a1 shows that the total amount of magmatic rock is ~300 km³/km at a convergence of 1100 km with subduction velocity of 5.0 cm/yr (model "Rvp5"). The predominant new crustal component is basalt, which is extracted by melting mantle peridotite. Granitic and dacitic components extracted from subducted crust and sediments contribute less than 50 km³/km. Figure 8b1 shows that the amount of magmatic rock is ~370 km³/km for the same convergence amount but with a subduction velocity of 3.0 cm/yr (model "Rvp3"). The main component is also basalt; however, the granitic and dacitic components are much more important than with the higher subduction rate, with granite contributing ~130 km³/km and dacite ~50 km³/km. With an even slower subduction rate of 2.0 cm/yr (model "Rvp2"; Figure 8c1), the total amount of magmatic rock is even higher, exceeding 400 km³/km at the same convergence of 1100 km, of which the granitic and dacitic fractions are no higher. Here we conclude that the slower the subduction velocity, the longer the subducted crust and sediments have to develop in the mantle wedge and partially melt to generate dacitic and granitic crust.

[36] The onset of major crustal production as indicated by the start point **SP** also varies greatly with subduction velocity: a higher subduction velocity results in an earlier (in terms of both convergence and time) **SP** because more water is taken into the mantle wedge and causes hydration of mantle atop the subducting slab and melting of hydrous mantle. The **SP** points are, respectively, at 200 km (Figure 8a1), 300 km (Figure 8b1), 450 km (Figure 8c1) convergence for subduction velocities of 5.0 cm/yr, 3.0 cm/yr, and 2.0 cm/yr. The plots of crustal addition rate versus convergence emphasize these
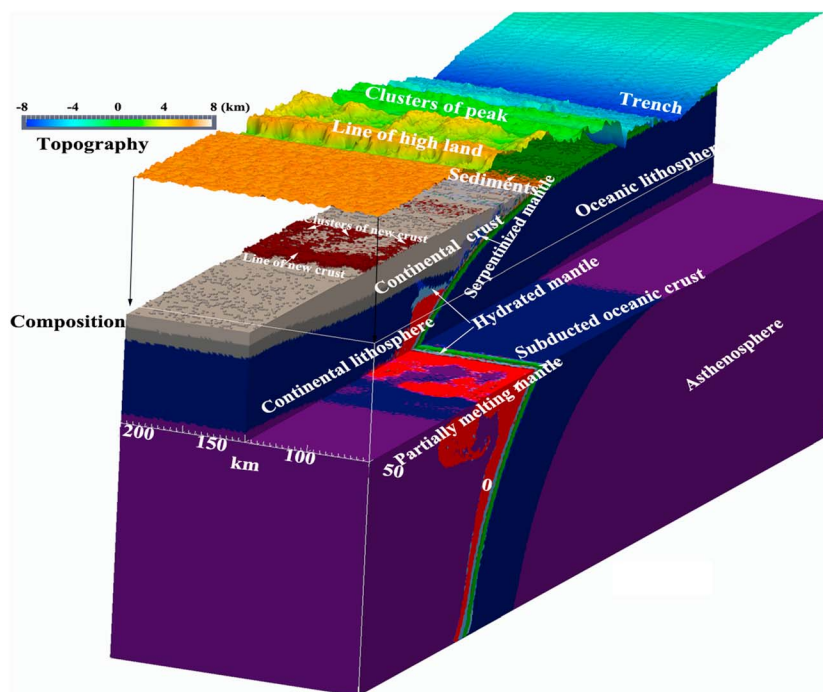
Figure 10. (Top) Three-dimensional topographic pattern and (below) clipped composition field at 27 Myr after the beginning of the model calculation) for model "Rvp65." Three-dimensional topographic patterns express the features of new crust formation. The extent of the partially molten mantle region corresponds to the horizontal extent of newly formed crust. Colors of composition: light grey: upper continental crust, orange: sediments; dark grey: lower continental crust; green: basalt; dark green: gabbro; red: partially molten mantle; blue: serpentinite; light blue: hydrated mantle; brown: new crust; violet: dry mantle.

values of **SP** (Figures 8(d–f)1). A common feature is that the crustal addition rate increases in a roughly linear manner until it reaches a critical point (**CP**), which occurs at ~700 km convergence for all velocities (Figures 8(d–f)1); just after CP, it starts to fluctuate within a range of values (20–25 km^3/km/Myr, 15–25 km^3/km/Myr in Figures 8(d–f)1), even in the cases with a lower melt extraction efficiency shown in the right panel of Figures 8(d–f)2.

[37] Lower melt extraction efficiency (Mmax = 6% and Mmin = 3%) influences the crustal addition rate and the relative fractions of the different crustal components (compare left and right parts in Figure 8). A lower melt extraction efficiency allows the melts to remain longer in the mantle wedge before extraction, thus creating favorable conditions for subducted sediments and oceanic crust to develop in the partially molten mantle plumes. For the fastest subduction velocity of 5 cm/yr (case "Brvp5"), Figure 8a2 shows that the amount of granitic crust increases to 100 km^3/km at 1100 km convergence—much higher than the ~40 km^3/km observed in Figure 8a1. At the slowest subduction rate and highest extraction threshold (model "Brvp2"), Figure 8c2 shows that granite crust is the main component at convergence amounts between 600 and 800 km. Higher extraction threshold also delays **SP** and **CP**, with the general characteristics of the crustal production rate graphs remaining qualitatively similar. It shows that lower melt extraction efficiency indeed enhances the probability of episodic extraction [*Schmeling*, 2006] seen from the smoother curves in Figures 8d1, 8e1, and 8f1 and big jumps in the curves in Figures 8d2, 8e2, and 8f2.

4. Discussion

[38] This 3-D study can be regarded as a successor to previous 2-D studies on crustal growth [*Nikolaeva et al.*, 2008; *Gerya and Meilick*, 2011; *Vogt et al.*, 2012], to investigate lateral variations in newly formed crust and the corresponding dynamics of the mantle wedge. Our study focuses on 3-D stable subduction under an active margin, one of the regimes identified in *Gerya and Meilick* [2011] and *Vogt et al.* [2012]. Generally, our results are consistent with a relatively low magmatic addition rate (such as 20 km^3/km/Myr) and different sources of new crust, including melting of the crustal part of the slab and melting of hydrated mantle shown in a 2-D stable arc setting [*Gerya and Meilick*, 2011; *Vogt et al.*, 2012]. The crustal addition rate in 3-D is around 10–30 km^3/km/Myr and has a tendency to fluctuate, which indicates the probability of episodic crustal growth in nature. Our results show that granitic and dacitic melts dominate crustal growth in the early stages (before **SP**). Basaltic melts extracted from partially molten peridotite start to dominate crustal growth at a later stage (after **SP**). The volume fraction of granitic-dacitic crust remains significant and varies from 15% to 50% depending on subduction rate (Figure 8). Indeed, the average andesitic bulk composition of new continental crust is not obtained in most of the models, implying more complex melt production and differentiation processes in natural arc settings [e.g., *Nye and Turner*, 1990; *Rudnick*, 1995; *Kodaira et al.*, 2006; *Castro and Gerya*, 2008; *Castro et al.*, 2009, 2010; *Hacker et al.*, 2011; *Straub et al.*, 2011].

4.1. Comparison With Linear Melting Model for Hydrous Mantle

[39] In order to understand the influence of different melting models, we also perform selected experiments (Rvp5lin, Rvp3lin, and Rvp2lin) with a water-saturated P-T dependent linear melting model for hydrous mantle [*Zhu et al.*, 2009, 2011a] instead of the model of *Katz et al.* [2003] used in other experiments. Results for the case with a subduction velocity of 3 cm/yr ("Rvp3lin") are shown in Figure 9, for comparison with Figures 8b1 and 8e1. The linear melting model dramatically overestimates the degree of hydrous mantle melting and the amount of extracted basaltic melt due to the water-saturation assumption [*Plank and Langmuir*, 1988]. The total volume of crust increases rapidly after **SP** and is five to six times more than that calculated using the "Katz melting model." The crustal addition rate (Figure 9b) increases linearly to **CP** with 170 km^3/km/Myr and then decreases linearly toward zero due to the decreasing contribution from partially molten peridotite been gradually compensated by increasing recycling of the new crust into the subduction zone (i.e., by subduction erosion of the new crust).

4.2. Possible Applications to Nature

[40] Topography responds directly to magmatic activities at surface. In a simplified way, in our 3-D model, new crust is assumed to erupt on the surface after melt extraction without considering plutonic emplacement underneath continental crust as in most recent 2-D studies [*Vogt et al.*, 2012]. Erosion is also neglected; thus, the magnitude of topography is overestimated. However, the topographic response to new crust is still obvious. Figure 10 shows the lithological field and its corresponding topography for the reference model "Rvp65" at 27 Myr since the beginning of model calculation. It shows three key points:

[41] 1. The plumes of partially molten peridotite are the dominant contributors to clusters of new crustal growth in mature subduction. In addition, temporal variations in new crust thickness/topography related to melt generation at subduction zones are characterized by timescales of 10s of millions of years, as found in nature [e.g., *Straub*, 2003]. The timescale is somewhat longer than the active lifetime (2–7 Myr) of thermal-chemical plumes estimated from our previous 3-D subduction models that neglected melt extraction processes [*Zhu et al.*, 2009, 2011a], but much less than the 100 Myr in *Hall* [2012].

[42] 2. Two trench-parallel lines of new crust are located 120–250 km away from the trench. This characteristic is quite common in our models. The line close to the trench displays a clustered pattern along strike, which reflects the roots of the plumes at depth. The line farther from the trench is more constant along strike, which reflects the heads of the underplating plumes [*Zhu et al.*, 2009]. In nature, two parallel lines of arc magmatism/batholiths can also be found, although there are different proposed driving mechanisms of formation; examples are Tertiary arc magmatic units in the Cordillera region of Ecuador [*Schütte et al.*, 2010], igneous outcrops in northwest Mexico and batholith of the coastal Sonora [*Ramos-Velazquez et al.*, 2008], and northeast Japan [*Zhao et al.*, 2002; *Tamura et al.*, 2002]. Another possible natural example may concern two parallel volcanic belts in Northland Peninsula in New Zealand [e.g., *Mortimer et al.*, 2007;

Schellart, 2007; *Booden et al.*, 2011; *Schellart*, 2012], where several other controversial driving mechanisms have already been proposed to explain the volcanism [e.g., *Herzer*, 1995; *Schellart*, 2012; *Crawford et al.*, 2003].

[43] 3. New crust is responsible for the development of topography. Our models consistently predict spatial clustering of the crustal growth and topography variation with characteristic wavelengths of 30–80 km, comparable to clustering of volcanoes in subduction-related arcs [e.g., *Honda and Yoshida*, 2005; *Zhu et al.*, 2009]. Reasons for this clustering might be the lateral variations of mobile water released by the subducting slab under conditions of water-induced gravitational instability and related temperature variations in the mantle wedge [e.g., *Gerya and Yuen*, 2003b; *Gerya et al.*, 2006; *Zhu et al.*, 2009; *Honda et al.*, 2010]. Cases with a subduction velocity of 5–6.5 cm/yr produce new crust/topography clustering with a wavelength of 50–70 km, and the setting is comparable to the distribution of volcanoes in the southern Alaska subduction zone and highlands developed in the back-arc region. However, southern Alaska subduction does not have the second volcanic belt found in some of our models. We speculate that in nature, melt extraction and transport in the mantle wedge are likely to be more complex compared to our models.

[44] Seismic structure provides information on the thermal [e.g., *Tamura et al.*, 2002] and/or chemical [e.g., *Jung and Karato*, 2001] anomalies and dynamics of the subduction zone. Low seismic velocity is generally interpreted as due to the presence of fluids/melts in the mantle wedge due to dehydration of the subduction slab and hydration processes in the mantle wedge [e.g., *Kissling and Lahr*, 1991; *Zhao*, 2001; *Syracuse and Abers*, 2006]. *Gerya et al.* [2006] used a coupled 2-D petrological-thermomechanical model to explain the strong seismic velocity variations existing beneath volcanic arcs [e.g., *Zhao*, 2001].

[45] It is widely accepted that b-value studies, that is, frequency-magnitude distribution analysis of local earthquakes [*Aki*, 1965; *Utsu*, 1966; *Shi and Bolt*, 1982], can image the source of magma [*Wiemer and Benoit*, 1996; *Wyss et al.*, 2001]. More recently, a combined approach of 3-D high-resolution Vp and Vs independent tomography and b-value study in the southern Alaska subduction zone shows clustered anomalies of high b-value and Vp/Vs ratio atop subducting slab [*van Stiphout et al.*, 2009], which correlate well with results of this study: clustering in space and time. In section A2, we show that hydrated plumes in the mantle wedge are characterized by high Vp/Vs ratios (Figures A1, A2, and A3), which are even higher than suggested by seismic data [e.g., *van Stiphout et al.*, 2009], but are within the realistic range [*Wang et al.*, 2012]. Such seismic effects are mainly caused by water and melts present in the mantle wedges.

[46] In our present study, fluid markers are used to track water release and fluid migration in the mantle wedge in order to give insights into the source and path of fluids in our simulations. The water release rate provides information about the source of fluids and mobile water concentration provides the information of the path of the fluids as shown in Figures 6 and 7. *van Stiphout et al.* [2009] infer plumes of rising fluids starting from the top of the slab at around 100 km depth and elaborate that dehydration of minerals is a major role for high b-values. Such plumes of mobile water are also found in our models, as visible in Figures 6 and 7.

They proposed that preexisting cracks and fissures in initially homogeneous oceanic crust are important factors for clustering of the arc volcanoes. Our initial model with a homogeneous oceanic crust without preexisting cracks and fissures can also produce volcanoes in clusters due to spontaneous clustering of dehydration and melting processes above the slabs driven by water-induced buoyancy in the mantle wedge [e.g., *Zhu et al.*, 2009, 2011a, 2011b; *Honda et al.*, 2010]. That means, preexisting cracks are not a prerequisite for volcanic clustering when we take into account the role of fluid in the subduction zone.

5. Conclusions

[47] We have for the first time modeled and investigated 4-D crustal growth processes in subduction-related arcs using 3-D petrological-thermomechanical models of subduction under an active continental margin. Subduction is implemented by an imposed convergence of the oceanic plate to the continental plate and spontaneous slab bending. The model accounts for dehydration of subducted crust, aqueous fluid transport, P-T-water content-dependent melting mode of hydrous mantle based on *Katz et al.* [2003], and instantaneous melt extraction once the melt fraction reaches a certain threshold. Due to the young oceanic lithosphere (30 Myr) used in our model, our results are more appropriate for explaining young/warm subduction zones, like the Southern Alaska subduction zone.

[48] The results show the following key points.

[49] 1. Crustal growth at a 3-D active margin is variable in both space and time. Clusters of newly formed crust are distributed in a linear pattern parallel to the trench (Figures 4 and 5). Model topography also expresses 2-D features in response to newly formed crust (see Figure 10). The characteristic wavelength of variations in crustal thickness and topography along the arc is on the order of 30–80 km and comparable to volcanoes clustering in natural arcs.

[50] 2. The clusters of new crust are mainly comprised of basalt episodically extracted from partially molten peridotite due to lateral variation of water release and mobile water content in the mantle wedge.

[51] 3. The total amount of newly formed crust correlates mainly with the amount of convergence since the beginning of subduction and is not strongly influenced by the plate convergence velocity.

[52] 4. Convergence velocity influences crustal composition in terms of the granitic-dacitic to basaltic crust ratio. This ratio is higher (up to 1:1) for slower subduction or a relatively low melt extraction efficiency (i.e., high melt extraction threshold). The maximum of crustal addition rate (25–40 km^3/km/Myr) occurs at around 700 km of convergence.

[53] 5. Our model with 6.5 cm/yr subduction velocity is comparable to the Southern Alaska subduction zone, and we obtain plumes of mobile water that resemble the plumes of rising fluids inferred from the seismological study of *van Stiphout et al.* [2009]. Partially molten plumes might be comparable to spatial clustering expressed in volcanism and in seismic anomalies in the Southern Alaska mantle wedge, which are now correlated with 4-D numerical modeling in spatial and temporal clustering. The water release rate could reflect the observed distribution of high Vp/Vs ratio and b-values atop the slab.

References

Aki, K. (1965), A note on use of microseisms in determining shallow structures of the Earth's crust, *Geophysics*, *30*(4), 665–666, doi:10.1190/1.1439640.

Albarede, F. (1998), The growth of continental crust, *Tectonophysics*, *296*, 1–14, doi:10.1016/S0040-1951(98)00133-4.

Allegre, C. J., and D. B. Othman (1980), Nd-Sr Isotopic Relationship in Granitoid Rocks and Continental-Crust Development - a Chemical Approach to Orogenesis, *Nature*, *286*, 335–342, doi:10.1038/286335a0.

Aramaki, S., and T. Ui (1978), Major element frequency distribution of the Japanese Quaternary volcanic rocks, *Bull. Volcanol.*, *41*, 390–407.

Arcay, D., E. Tric, and M. P. Doin (2005), Numerical simulations of subduction zones - Effect of slab dehydration on the mantle wedge dynamics, *Phys. Earth Planet. Inter.*, *149*, 133–153, doi:10.1016/J.Pepi.2004.08.020.

Bittner, D., and H. Schmeling (1995), Numerical Modeling of Melting Processes and Induced Diapirism in the Lower Crust, *Geophys. J. Int.*, *123*, 59–70, doi:10.1111/J.1365-246x.1995.Tb06661.X.

Booden, M. A., I. E. M. Smith, P. M. Black, and J. L. Mauk (2011), Geochemistry of the Early Miocene volcanic succession of Northland, New Zealand, and implications for the evolution of subduction in the Southwest Pacific, *J. Volcanol. Geoth. Res.*, *199*, 25–37, doi:10.1016/J.Jvolgeores.2010.10.006.

Bostock, M. G., R. D. Hyndman, S. Rondenay, and S. M. Peacock (2002), An inverted continental Moho and serpentinization of the forearc mantle, *Nature*, *417*, 536–538, doi:10.1038/417536a.

Cagnioncle, A. M., E. M. Parmentier, and L. T. Elkins-Tanton (2007), Effect of solid flow above a subducting slab on water distribution and melting at convergent plate boundaries, *J. Geophys. Res.*, *112*, B09402, doi:10.1029/2007JB004934.

Carlson, R. L., and D. J. Miller (2003), Mantle wedge water contents estimated from seismic velocities in partially serpentinized peridotites, *Geophys. Res. Lett.*, *30*(5), 1250, doi:10.1029/2002GL016600.

Castro, A., and T. V. Gerya (2008), Magmatic implications of mantle wedge plumes: Experimental study, *Lithos*, *103*(1-2), 138–148, doi:10.1016/J.Lithos.2007.09.012.

Castro, A., A. Garcia-Casco, C. Fernandez, L. G. Corretge, I. Moreno-Ventas, T. Gerya, and I. Low (2009), Ordovician ferrosilicic magmas: Experimental evidence for ultrahigh temperatures affecting a metagreywacke source, *Gondwana Res.*, *16*, 622–632, doi:10.1016/J.Gr.2008.12.011.

Castro, A., T. Gerya, A. Garcia-Casco, C. Fernandez, J. Diaz-Alvarado, I. Moreno-Ventas, and I. Low (2010), Melting Relations of MORB-Sediment Melanges in Underplated Mantle Wedge Plumes; Implications for the Origin of Cordilleran-type Batholiths, *J. Petrol.*, *51*(6), 1267–1295, doi:10.1093/Petrology/Egq019.

Clauser, C., and E. Huenges (1995), Thermal conductivity of rocks and minerals, in *Rock Physics and Phase Relations*, AGU Ref. Shelf, vol. *3*, edited by T. J. Ahrens, pp. 105–126, AGU, Washington, D. C., doi:10.1029/RF003p0105.

Connolly, J. A. D. (2005), Computation of phase equilibria by linear programming: A tool for geodynamic modeling and its application to subduction zone decarbonation, *Earth Planet. Sci. Lett.*, *236*, 524–541, doi:10.1016/J.Epsl.2005.04.033.

Connolly, J. A. D., M. W. Schmidt, G. Solferino, and N. Bagdassarov (2009), Permeability of asthenospheric mantle and melt extraction rates at mid-ocean ridges, *Nature*, *462*, 209–214, doi:10.1038/nature08517.

Crameri, F., P. J. Tackley, I. Meilick, T. V. Gerya, and B. J. P. Kaus (2012), A free plate surface and weak oceanic crust produce single-sided subduction on Earth, *Geophys. Res. Lett.*, *39*, L03306, doi:10.1029/2011GL050046.

Crawford, A. J., S. Meffre, and P. A. Symonds (2003), 120 to 0 Ma tectonic evolution of the southwest Pacific and analogous geological evolution of the 600 to 220 Ma Tasman fold belt system, *Geol. Soc. Australia Spec. Publ.*, *22*, 377–397.

Dimalanta, C., A. Taira, G. P. Yumul, H. Tokuyama, and K. Mochizuki (2002), New rates of western Pacific island arc magmatism from seismic and gravity data, *Earth Planet. Sc. Lett.*, *202*, 105–115, doi:10.1016/S0012-821x(02)00761-6.

Eiler, J. M., M. J. Carr, M. Reagan, and E. Stolper (2005), Oxygen isotope constraints on the sources of Central American arc lavas, *Geochem. Geophys. Geosyst.*, *6*, Q07007, doi:10.1029/2004GC000804.

Elliott, T., T. Plank, A. Zindler, W. White, and B. Bourdon (1997), Element transport from slab to volcanic front at the Mariana arc, *J. Geophys. Res.*, *102*(B7), 14,991–15,019, doi:10.1029/97JB00788.

England, P. C., and R. F. Katz (2010), Melting above the anhydrous solidus controls the location of volcanic arcs, *Nature*, *467*, 700–703, doi:10.1038/nature09417.

Faccenda, M., T. V. Gerya, and L. Burlini (2009), Deep slab hydration induced by bending related variations in tectonic pressure, *Nat. Geosci.*, *2*, 790–793, doi:10.1038/Ngeo656.

Faccenda, M., T. V. Gerya, N. S. Mancktelow, and L. Moresi (2012), Fluid flow during slab unbending and dehydration: Implications for intermediate-depth seismicity, slab weakening and deep water recycling, *Geochem. Geophys. Geosyst.*, *13*, Q01010, doi:10.1029/2011GC003860.

Farris, D. W. (2010), Tectonic and petrologic evolution of the Kodiak batholith and the trenchward belt, Kodiak Island, AK: Contact fault juxtaposition? *J. Geophys. Res.*, *115*, B07208, doi:10.1029/2009JB006434.

Faul, U. H. (2001), Melt retention and segregation beneath mid-ocean ridges, *Nature*, *410*(6831), 920–923, doi:10.1038/35073556.

Gerya, T. V., and F. I. Meilick (2011), Geodynamic regimes of subduction under an active margin: effects of rheological weakening by fluids and melts, *J. Metamorph. Geol.*, *29*, 7–31, doi:10.1111/j.1525-1314.2010.00904.x.

Gerya, T. V., and D. A. Yuen (2003a), Characteristics-based marker-in-cell method with conservative finite-differences schemes for modeling geological flows with strongly variable transport properties, *Phys. Earth Planet. Inter.*, *140*, 293–318, doi:10.1016/j.pepi.2003.09.006.

Gerya, T. V., and D. A. Yuen (2003b), Rayleigh-Taylor instabilities from hydration and melting propel "cold plumes" at subduction zones, *Earth Planet. Sci. Lett.*, *212*, 47–62, doi:10.1016/S0012-821x(03)00265-6.

Gerya, T. V., and D. A. Yuen (2007), Robust characteristics method for modeling multiphase visco-elasto-plastic thermo-mechanical problems, *Phys. Earth Planet. Inter.*, *163*, 83–105, doi:10.1016/J.Pepi.2006.02.005.

Gerya, T. V., J. A. D. Connolly, D. A. Yuen, W. Gorczyk, and A. M. Capel (2006), Seismic implications of mantle wedge plumes, *Phys. Earth Planet. Inter.*, *156*, 59–74, doi:10.1016/J.Pepi.2006.02.005.

Gerya, T. V., J. A. D. Connolly, and D. A. Yuen (2008), Why is terrestrial subduction one-sided?, *Geology*, *36*, 43–46, doi:10.1130/G24060a.1.

Gorczyk, W., A. P. Willner, T. V. Gerya, J. A. D. Connolly, and J.-P. Burg (2007), Physical controls of magmatic productivity at Pacific-type convergent margins: numerical modelling, *Phys. Earth Planet. Inter.*, *163*, 209–232, doi:10.1016/J.Pepi.2007.05.010.

Green, T. H. (1980), Island arc and continent-building magmatism – review of petrogenic models based on experimental petrology and geochemistry, *Tectonophysics*, *63*, 367–385, doi:10.1016/0040-1951(80)90121-3.

Grove, T. L., N. Chatterjee, S. W. Parman, and E. Médard (2006), The influence of H2O on mantle wedge melting, *Earth Planet. Sci. Lett.*, *249*, 74–89, doi:10.1016/j.epsl.2006.06.043.

Grove, T. L., C. B. Till, E. Lev, N. Chatterjee, and E. Medard (2009), Kinematic variables and water transport control the formation and location of arc volcanoes, *Nature*, *459*, 694–697, doi:10.1038/nature08044.

Hacker, B. R., P. B. Kelemen, and M. D. Behn (2011), Differentiation of the continental crust by relamination, *Earth Planet. Sci. Lett.*, *307*, 501–516, doi:10.1016/J.Epsl.2011.05.024.

Hall, P. S. (2012), On the thermal evolution of the mantle wedge at subduction zones, *Phys. Earth Planet. Inter.*, *198*, 9–27, doi:10.1016/J.Pepi.2012.03.004.

Hall, P. S., and C. Kincaid (2001), Diapiric flow at subduction zones: A recipe for rapid transport, *Science*, *292*, 2472–2475, doi:10.1126/Science.1060488.

Hawkesworth, C. J., and A. I. S. Kemp (2006), Evolution of the continental crust, *Nature*, *443*, 811–817, doi:10.1038/Nature05191.

Hawkesworth, C. J., S. P. Turner, F. McDermott, D. W. Peate, and P. van Calsteren (1997), UTh isotopes in arc magmas:implications for element transfer from the subducted crust, *Science*, *276*, 551–555, doi:10.1126/Science.276.5312.551.

Hebert, L. B., P. Antoshechkina, P. Asimow, and M. Gurnis (2009), Emergence of a low-viscosity channel in subduction zones through the coupling of mantle flow and thermodynamics, *Earth Planet. Sci. Lett.*, *278*, 243–256, doi:10.1016/J.Epsl.2008.12.013.

Herzer, R. H. (1995), Seismic Stratigraphy of a Buried Volcanic Arc, Northland, New-Zealand and Implications for Neogene Subduction, *Mar. Petrol. Geol.*, *12*(5), 511–531, doi:10.1016/0264-8172(95)91506-K.

Hess, P. C. (1989), *Origin of Igneous Rocks*, Harward Univ. Press, London, UK.

Hirschmann, M. M. (2000), Mantle solidus: experimental constraints and the effects of peridotite composition, *Geochem. Geophys. Geosyst.*, doi:10.1029/2000GC000070.

Hofmeister, A. M. (1999), Mantle Values of Thermal Conductivity and the Geotherm from Phonon Lifetimes, *Science*, *283*, 1699–1706, doi:10.1126/science.283.5408.1699.

Holbrook, W. S., D. Lizarralde, S. McGeary, N. Bangs, and J. Diebold (1999), Structure and composition of Aleutian island arc and implications for crustal growth, *Geology*, *27*, 31–34.

Honda, S., and T. Yoshida (2005), Application of the model of small-scale convection under the island arc to the NE Honshu subduction zone, *Geochem. Geophys. Geosyst.*, *6*, Q01002, doi:10.1029/2004GC000785. (Correction, *Geochem. Geophys. Geosyst.*, 6, Q06004, doi:10.1029/2005GC000985, 2005.)

Honda, S., T. Yoshida, and K. Aoike (2007), Spatial and temporal evolution of arc volcanism in the northeast Honshu and Izu-Bonin arcs: Evidence of small-scale convection under the island arc?, *Isl. Arc*, *16*, 214–223, doi:10.1111/j.1440-1738.2007.00567.x.

Honda, S., T. Gerya, and G. Zhu (2010), A simple three-dimensional model of thermo–chemical convection in the mantle wedge, *Earth Planet. Sci. Lett.*, *290*, 311–318, doi:10.1016/J.Epsl.2009.12.027.

Iwamori, H. (1998), Transportation of H2O and melting in subduction zones, *Earth Planet. Sci. Lett.*, *160*, 65–80, doi;10.1016/S0012-821x(98)00080-6.

Johannes, W. (1985), The significance of experimental studies for the formation of migmatites, in *Migmatites*, edited by J. R. Ashworth, Blackie, Glasgow, UK, pp. 36–85.

Jung, H., and S. Karato (2001), Water-induced fabric transitions in Olivine, *Science*, *293*, 1460–1463, doi:10.1126/Science.1062235.

Katz, R. F., M. Spiegelman, and C. H. Langmuir (2003), A new parameterization of hydrous mantle melting, *Geochem. Geophys. Geosyst.*, *4*(9), 1073, doi:10.1029/2002GC000433.

Kelley, K. A., T. Plank, T. L. Grove, E. M. Stolper, S. Newman, and E. Hauri (2006), Mantle melting as a function of water content beneath back-arc basins, *J. Geophys. Res.*, *111*, B09208, doi:10.1029/2005JB003732.

Kimura, J., and T. Yoshida (2006), Contributions of slab fluid, mantle wedge and crust to the origin of quaternary lavas in the NE Japan arc, *J. Petrol.*, *47*, 2185–2232, doi:10.1093/Petrology/Egl041.

Kissling, E., and J. Lahr (1991), Tomographic image of the Pacific slab under southern Alaska, *Eclogae Geol. Helv.*, *84*(2), 297–315.

Kodaira, S., T. Sato, N. Takahashi, A. Ito, Y. Tamura, Y. Tatsumi, and Y. Kaneda (2006), Seismological evidence for variable growth of crust along the Izu intraoceanic arc, *J. Geophys. Res.*, *112*, B05104, doi:10.1029/2006JB004593.

Kodaira, S., T. Sato, N. Takahashi, S. Miura, Y. Tamura, Y. Tatsumi, and Y. Kaneda (2007), New seismological constraints on growth of continental crust in the Izu-Bonin intra-oceanic arc, *Geology*, *35*, 1031–1034, doi:10.1130/G23901a.1.

Lahitte, P., A. Samper, and X. Quidelleur (2012), DEM-based reconstruction of southern Basse-Terre volcanoes (Guadeloupe archipelago, FWI): Contribution to the Lesser Antilles Arc construction rates and magma production, *Geomorphology*, *136*, 148–164, doi:10.1016/J.Geomorph.2011.04.008.

Maxeine, R. O., and N. Rayner (2011), Continental arc magmatism along the southeast Hearne Craton margin in Saskatchewan, Canada: Comparison of the 1.92–1.91 Ga Porter Bay Complex and the 1.86–1.85 Ga Wathaman Batholith, *Precambrian Res.*, *184*, 93–120, doi:10.1016/J.Precamres.2010.10.005.

Mortimer, N., R. H. Herzer, P. B. Gans, C. Laporte-Magoni, A. T. Calvert, and D. Bosch (2007), Oligocene–Miocene tectonic evolution of the South Fiji Basin and Northland Plateau, SW Pacific Ocean: evidence from petrology and dating of dredged rocks, *Mar. Geol.*, *237*, 1–24, doi:10.1016/j.margeo.2006.10.033.

Mortimer, N., P. B. Gans, J. M. Palin, S. Meffre, and R. Herzer (2010), Location and migration of Miocene-Quaternary volcanic arcs in the SW Pacific region, *J. Volcanol. Geoth. Res.*, *190*, 1–10, doi:10.1016/J.Jvolgeores.2009.02.017.

Nakajima, J., and A. Hasegawa (2003a), Estimation of thermal structure in the mantle wedge of northeastern Japan from seismic attenuation data, *Geophys. Res. Lett.*, *30*, 1760, doi:10.1029/2003GL017185.

Nakajima, J., and A. Hasegawa (2003b), Tomographic imaging of seismic velocity structure in and around the Onikobe volcanic area, northeastern Japan: implications for fluid distribution, *J. Volcanol. Geotherm. Res.*, *127*, 1–18, doi:10.1016/S0377-0273(03)00155-0.

Naliboff, J. B., M. I. Billen, T. Gerya, and J. Saunders (2013), Dynamics of outer rise faulting in oceanic-continental subduction systems, *Geochem. Geophys. Geosyst.*, *14*, doi:10.1002/ggge.20155.

Nikolaeva, K., T. V. Gerya, and J. A. D. Connolly (2008), Numerical modelling of crustal growth in intraoceanic volcanic arcs, *Phys. Earth Planet. Inter.*, *171*, 336–356, doi:10.1007/Bf00334805.

Nye, C. J., and D. L. Turner (1990), Petrology, geochemistry, and age of the spurr volcanic complex, eastern aleutian arc, *B. Volcanol.*, *52*, 205–226, doi:10.1007/Bf00334805.

Nye, C. J., S. E. Swanson, V. F. Avery, and T. P. Miller (1994), Geochemistry of the 1989-1990 eruption of redoubt volcano. 1. whole-rock major- and trace-element chemistry, *J. Volcanol. Geotherm. Res.*, *62*, 429–452, doi:10.1016/0377-0273(94)90046-9.

Nye, C. J., M. L. Harbin, T. P. Miller, S. E. Swanson, and C. A. Neal (1995), Whole rock major- and trace-element chemistry of 1992 ejectafrom Crater Peak, Mount Spurr Volcano, Alaska. In: "The 1992 eruptions of Crater Peak vent, Mount Spurr Volcano,Alaska.". TEC Keith, *US Geol Surv Bull*. 2139: 119-128.

Peacock, S. M. (1990), Fluid processes in subduction zones, *Science*, *248*, 329–337, doi:10.1126/Science.248.4953.329.

Plank, T., and C. H. Langmuir (1988), An evaluation of the global variations in the major element chemistry of arc basalts, *Earth Planet. Sci.Lett.*, *90*, 349–370, doi:10.1016/0012-821x(88)90135-5.

Poli, S., and M. W. Schmidt (2002), Petrology of subducted slabs, *Annu. Rev. Earth Planet. Sci.*, *30*, 207–235, doi:10.1146/annurev.earth.30.091201.140550.

Ramos-Velazquez, E., T. Calmus, V. Valencia, A. Iriondo, M. Valencia-Moreno, and H. Bellon (2008), U-Pb and 40Ar/39Ar geochronology of the coastal Sonora batholith: New insights on Laramide continental arc magmatism, *Revista Mexicana de Ciencias Geológicas*, *25*(2), 314–333.

Ranalli, G. (1995), *Rheology of the Earth: Deformation and Flow Processes in Geophysics and Geodynamics*, 2nd ed., 23 pp., Chapman and Hall, Boston, Mass.

Reymer, A., and G. Schubert (1984), Phanerozoic addition rates to the continental crust and crustal growth, *Tectonics*, *3*(1), 63–77, doi:10.1029/TC003i001p00063.

Ringwood, A. E. (1990), Slab–mantle interactions: 3. Petrogenesis of intra-plate magmas and structure of the upper mantle, *Chem. Geol.*, *82*, 187–207, doi:10.1016/0009-2541(90)90081-H.

Roman, D. C., K. V. Cashman, C. A. Gardner, P. J. Wallace, and J. J. Donovan (2006), Storage and interaction of compositionally heterogeneous magmas from the 1986 eruption of Augustine Volcano, Alaska, *B. Volcanol.*, *68*(3), 240–254, doi:10.1007/S00445-005-0003-Z.

Rudnick, R. L. (1995), Making continental crust, *Nature*, *378*, 571–577.

Rudnick, R. L., and S. Gao (2003), Composition of the continental crust, in *The Crust. Treatise on Geochemistry*, edited by R. L. Rudnick, pp. 1–64, Elsevier-Pergamon, Oxford.

Schellart, W. P. (2007), Northeastward subduction followed by slab detachment to explain ophiolite obduction and Early Miocene volcanism in Northland, New Zealand, *Terra Nova*, *19*, 211–218, doi:10.1111/j1365-3121.2007.00736.x.

Schellart, W. P. (2012), Comment on "Geochemistry of the Early Miocene volcanic succession of Northland, New Zealand, and implications for the evolution of subduction in the Southwest Pacific" by MA Booden, IEM Smith, PM Black and JL Mauk, *J. Volcanol. Geotherm. Res.*, *211*, 112–117, doi:10.1016/j.jvolgeores.2011.10.010.

Schmeling, H. (2006), A model of episodic melt extraction for plumes. *J. Geophys. Res.*, *111*, B03202, doi:10.1029/2004JB003423.

Schmeling, H., et al. (2008), A benchmark comparison of spontaneous subduction models – towards a free surface, *Phys. Earth Planet. Inter.*, *171*, 198–223, doi:10.1016/J.Pepi.2008.06.028.

Schmidt, M. W., and S. Poli (1998), Experimentally based water budgets for dehydrating slabs and consequences for arc magma generation, *Earth Planet. Sci. Lett.*, *163*, 361–379, doi:10.1016/S0012-821X(98)00142-3.

Schütte, P., M. Chiaradia, and B. Beate (2010), Geodynamic controls on Tertiary arc magmatism in Ecuador: Constraints from U–Pb zircon geochronology of Oligocene–Miocene intrusions and regional age distribution trends, *Tectonophysics*, *489*, 159–176, doi:10.1016/J.Tecto.2010.04.015.

Shi, Y., and B. Bolt (1982), The standard error of the magnitude-frequency b value, *Bull. Seismol. Soc. Am.*, *72*(5), 1677–1687.

Spiegelman, M., and D. McKenzie (1987), Simple 2-D models for melt extraction at mid-ocean ridges and island arcs, *Earth Planet. Sci. Lett.*, *83*, 137–152, doi:10.1016/0012-821X(87)90057-4.

Staudigel, H., S. R. Hart, and S. Richardson (1981), Alteration of the oceanic crust: processes and timing, *Earth Planet. Sci. Lett.*, *52*, 311–325, doi:10.1016/J.Epsl.2011.01.013.

Stern, R. J., and S. H. Bloomer (1992), Subduction zone infancy: Examples from the Eocene Izu-Bonin-Mariana and Jurassic California arcs, *Geol. Soc. Am. Bull.*, *104*, 1621–1636, doi:10.1130/0016-7606(1992)104 < 1621:Szieft > 2.3.Co;2.

van Stiphout, T., E. Kissling, S. Wiemer, and N. Ruppert (2009), Magmatic processes in the Alaska subduction zone by combined 3-D b value imaging and targeted seismic tomography, *J. Geophys. Res.*, *114*, B11302, doi:10.1029/2008JB005958.

Straub, S. M. (2003), The evolution of the Izu Bonin-Mariana volcanic arcs (NW Pacific) in terms of major element chemistry, *Geochem. Geophys. Geosyst.*, *4*(2), 1018, doi:10.1029/2002GC000357.

Straub, S. M., A. Gomez-Tuena, F. M. Stuart, G. F. Zellmer, R. Espinasa-Perena, Y. Cai, and Y. Iizuk (2011), Formation of hybrid arc andesites beneath thick continental crust, *Earth Planet. Sci. Lett.*, *303*, 337–347, doi:10.1016/J.Epsl.2011.01.013.

Syracuse, E., and G. Abers (2006), Global compilation of variations in slab depth beneath arc volcanoes and implications, *Geochem. Geophys. Geosyst.*, *7*, Q05017, doi:10.1029/2005GC001045.

Taira, A., et al. (1998), Nature and growth rate of the Northern Izu-Bonin (Ogasawara) arc crust and their implications for continental crust formation, *Isl. Arc*, *7*, 395–407, doi:10.1046/J.1440-1738.1998.00198.X.

Tamura, Y., Y. Tatsumi, D. P. Zhao, Y. Kido, and H. Shukuno (2002), Hot fingers in the mantle wedge: New insights into magma genesis in subduction zones, *Earth Planet. Sci. Lett.*, *197*, 105–116, doi:10.1016/S0012-821X(02)00465-X.

Tatsumi, Y. (1989), Migration of fluid phases and genesis of basalt magmas in subduction zones, *J. Geophys. Res.*, *94*, 4697–4707, doi:10.1029/Jb094ib04p04697.

Taylor, S. R. (1967), The origin and growth of continents, *Tectonophysics*, *4*, 17–34, doi:10.1016/0040-1951(67)90056-X.

Turcotte, D. L., and G. Schubert (2002), *Geodynamics*, Cambridge Univ. Press, Cambridge, UK.

Utsu, T. (1966), A statistical significance test of the difference in b value between two earthquake groups, *J. Phys. Earth*, *14*, 37–40.

van Keken, P. E., B. R. Hacker, E. M. Syracuse, and G. A. Abers (2011), Subduction factory: 4. Depth-dependent flux of H2O from subducting slabs worldwide, *J. Geophys. Res.*, *116*, B01401, doi:10.1029/2010JB007922.

Vogt, K., T. V. Gerya, and A. Castro (2012), Crustal growth at active continental margins: Numerical modeling, *Phys. Earth Planet. Inter.*, *192*, 1–20, doi:10.1016/J.Pepi.2011.12.003.

von Huene, R., and D. W. Scholl (1991), Observations at convergent mariging concerning sediment subduction, subduction erosion, and the growth of continental crust, *Rev. Geophys.*, *29*(3), 279–316, doi:10.1029/91RG00969.

Wang, X. Q., A. Schubnel, J. Fortin, E. C. David, Y. Gueguen, and H. K. Ge (2012), High Vp/Vs ratio: Saturated cracks or anisotropy effects?, *Geophys. Res. Lett.*, *39*, L11307, doi:10.1029/2012gl051742.

Wiemer, S., and J. P. Benoit (1996), Mapping the B-value anomaly at 100 km depth in the Alaska and New Zealand Subduction Zones, *Geophys. Res. Lett.*, *23*(13), 1557–1560, doi:10.1029/96GL01233.

Wyss, M., A. Hasegawa, and J. Nakajima (2001), Source and path of magma for volcanoes in the subduction zone of northeastern Japan, *Geophys. Res. Lett.*, *28*, 1819–1822, doi:10.1029/2000GL012558.

Zhao, D. (2001), Seismological structure of subduction zones and its implications for arc magmatism and dynamics, *Phys. Earth Planet. Inter.*, *127*, 197–214, doi:10.1016/S0031-9201(01)00228-X.

Zhao, D., O. P. Mishra, and R. Sanda (2002), Influence of fluids and magma on earthquakes: Seismological evidence, *Phys. Earth Planet. Inter.*, *132*, 249–267, doi:10.1016/S0031-9201(02)00082-1.

Zhu, G., T. V. Gerya, D. A. Yuen, S. Honda, T. Yoshida, and J. A. D. Connolly (2009), 3-D Dynamics of hydrous thermalchemical plumes in oceanic subduction zones, *Geochem. Geophys. Geosyst.*, *10*, Q11006, doi:10.1029/2009GC002625.

Zhu, G., T. V. Gerya, and D. Yuen (2011a), Influence of the buoyancy of Partially molten rock on 3-D plume patterns and melt productivity above retreating slabs, *Phys. Earth Planet. Inter.*, *185*, 112–121, doi:10.1016/j.pepi.2011.02.005.

Zhu, G., T. V. Gerya, and D. A. Yuen (2011b), Melt evolution above a spontaneously retreating subducting slab in a three-dimensional model, *J. Earth Sci.*, *22*, 137–142, doi:10.1007/S12583-011-0165-X.